

1 Atmospheric CO₂ dynamics in a coastal megacity: spatiotemporal 2 patterns, sea–land breeze impacts, and anthropogenic–biogenic 3 emission partitioning

4 Jinwen Zhang¹, Yongjian Liang², Chenglei Pei², Bo Huang³, Yingyan Huang², Xiufeng Lian^{1,3},
5 Shaojie Song⁴, Chunlei Cheng¹, Cheng Wu¹, Zhen Zhou¹, Junjie Li⁵, Mei Li^{1*}

6 ¹College of Environment and Climate, Institute of Mass Spectrometry and Atmospheric Environment, Guangdong
7 Provincial Engineering Research Center for Online Source Apportionment System of Air Pollution, Guangdong–
8 Hongkong–Macau Joint Laboratory of Collaborative Innovation for Environmental Quality, Jinan University,
9 Guangzhou 511443, China

10 ²Guangzhou Ecological and Environmental Monitoring Center Station, Guangdong, Guangzhou 510006, China

11 ³Guangzhou Hexin Instrument Co., Ltd., Guangdong, Guangzhou 510530, China

12 ⁴College of Environmental Science and Engineering, Nankai University, Tianjin 300350, China

13 ⁵School of Environment, Beijing Jiaotong University, Beijing 100044, China

14 *Correspondence to:* Mei Li (limei@jnu.edu.cn)

15 **Abstract.** Attributing observed carbon dioxide (CO₂) to fossil-fuel emissions versus biogenic fluxes is essential
16 for assessing urban mitigation, but in coastal megacities it is complicated by anthropogenic–biogenic coupling and
17 sea–land breeze (SLB) circulation. Here we analyze Guangzhou using multi-site in situ CO₂ and CO measurements
18 (January 2023–September 2024), transport footprints, and a site-specific $\Delta\text{CO}/\Delta\text{CO}_2$ (R_{CO}) relationship to resolve
19 spatiotemporal variability, quantify SLB effects, and partition fossil-fuel (CO₂ff) and biogenic (CO₂bio)
20 contributions without assimilating emission inventories. Along a coastal–urban–suburban gradient, the coastal site
21 shows the largest seasonal amplitude, the vegetated site exhibits strong summertime diurnal amplitude, and the
22 urban core is combustion-dominated. These gradients reveal a “coastal CO₂ dome” that—unlike urban domes often
23 conceptualized as core-anchored—is seasonally displaced, with peak concentrations shifting away from the core
24 due to the interplay of coastal ventilation and biogenic exchange. SLB effects are seasonal: SLB ventilates CO₂ in
25 spring–winter but promotes summertime accumulation (+2.08 ppm) under stable stratification, accompanied by
26 pronounced CO enhancements, consistent with trapped/recirculated combustion plumes. Regression-derived urban
27 R_{CO} is consistent with post-2013 broad tightening of coal/industrial and vehicle-emission controls. Winter-
28 afternoon urban CO₂ff attribution remains robust to transport-model configurations and measurement/background
29 uncertainty. Summer-afternoon CO₂bio shows substantial biogenic uptake, offsetting ~ 60 % of concurrent CO₂ff.
30 These results demonstrate that coastal dynamics and urban greening reshape observed CO₂ signals, highlighting
31 that biogenic–anthropogenic decoupling and SLB-aware sampling are essential for the robust evaluation of carbon
32 mitigation in coastal megacities.

33 **1 Introduction**

34 Atmospheric carbon dioxide (CO₂), the predominant anthropogenic driver of climate change, is accumulating at
35 unprecedented rates in human history (WMO, 2024). Future CO₂ increments will exert stronger warming effects
36 than equivalent past increases due to climate system feedbacks (He et al., 2023), making emission control
37 imperative. Despite covering only 3 % of global land, urban areas generate over 70 % of carbon emissions (Crippa
38 et al., 2021), positioning cities as critical arenas where mitigation policies, infrastructure transitions, and urban
39 greening can drive measurable changes in urban carbon budgets (WMO, 2025).

40

41 Urban atmospheric CO₂ concentrations provide a complementary constraint to flux- or inventory-based
42 assessments because they integrate surface emissions, biogenic exchange, and atmospheric transport over the
43 upwind source area (Lin et al., 2003; Shusterman et al., 2018; Pitt et al., 2022). This integration, however, creates
44 an attribution challenge because observed CO₂ variability reflects coupled effects of fossil-fuel emissions, biogenic
45 fluxes, and meteorology/transport, and thus is not uniquely attributable to any single driver, although one factor
46 may dominate in certain regimes, especially on diurnal to seasonal timescales (Xueref-Remy et al., 2018; Yang et
47 al., 2021; Mitchell et al., 2018). The challenge is particularly acute in coastal megacities, where land–sea thermal
48 contrasts and marine background inflow drive strong diurnal reversals in advection and boundary-layer structure
49 (Leroyer et al., 2014; Lei et al., 2024). These dynamics complicate observational representativeness and source–
50 sink separation, and can make inferred CO₂ enhancements sensitive to background selection under different
51 transport regimes (Verhulst et al., 2017). Given their high exposure to climate-related hazards, especially flooding
52 and storm impacts, coastal megacities are priority targets for climate-risk management, motivating robust, policy-
53 relevant CO₂ emissions assessment (Kumar, 2021).

54

55 A range of approaches has been used to constrain urban carbon budgets, including bottom-up inventories, tower-
56 based atmospheric observations, tracer/isotope measurements, and atmospheric inversions. Bottom-up inventories
57 provide essential baselines, yet urban emissions remain uncertain and can differ across products because they
58 depend on activity/emission-factor assumptions and proxy-based downscaling (Gately and Hutyra, 2017; Gurney
59 et al., 2019). While radiocarbon (¹⁴C) measurements provide robust fossil-fuel/biogenic partitioning (Turnbull et
60 al., 2015; Berhanu et al., 2017; Wang et al., 2022), their high cost and discontinuous sampling limit their
61 applicability for long-term, high-frequency monitoring. Similarly, eddy covariance (EC) measurements quantify
62 net CO₂ fluxes within tower footprints (typically 1–2 km radius), yet the derived flux partitioning reflects only
63 local-scale dynamics and cannot fully represent city-wide carbon exchange processes (Velasco et al., 2013; Menzer

64 and Mcfadden, 2017; Wu et al., 2022b). Fully three-dimensional (3-D) atmospheric inversions can assimilate
65 concentration data to estimate city-scale emissions and quantify posterior uncertainty when observation networks
66 adequately constrain boundary inflow and key transport uncertainties (Lauvaux et al., 2016; Lian et al., 2023). Yet
67 in practice, urban inversions are often limited by incomplete observational coverage, representativeness (sub-grid)
68 errors, and transport biases (Boon et al., 2016; Deng et al., 2017; Ye et al., 2020; Che et al., 2022b). They can also
69 remain sensitive to choices of background/boundary conditions and prior assumptions, including those related to
70 biogenic fluxes, which can be large and temporally variable during the growing season (Turnbull et al., 2018; Nalini
71 et al., 2022; Ye et al., 2020). These constraints motivate complementary observation-driven frameworks that
72 emphasize process-level interpretation of concentration variability while explicitly tracking uncertainty sources.

73

74 A defining coastal process is the sea–land breeze (SLB), a common mesoscale circulation driven by land–sea
75 thermal contrast (Shen et al., 2021). In the Pearl River Estuary (PRE), SLB occurrence shows pronounced
76 seasonality and spatial dependence, with spring–autumn maxima reported in parts of the region (You and Chi-Hung
77 Fung, 2019; Mai et al., 2024b). SLB produces a clear diurnal reversal between onshore and offshore flow and can
78 modify boundary-layer structure and mixing depth (Wu et al., 2013; Lei et al., 2024), complicating the
79 interpretation of urban CO₂ variability. By contrast, inland basins/valleys lack marine inflow–outflow and may be
80 shaped by lake–land breeze circulations (Yang et al., 2022) or other topography-modulated flows that can shift
81 background conditions and the footprint representativeness of urban observations (Mitchell et al., 2018; Wang et
82 al., 2021). Beyond the PRE, China’s coastal basins exhibit distinct SLB seasonality (e.g., a summer maximum in
83 the Bohai Rim, weak seasonality in the Yangtze River Delta, and an autumn maximum in the PRE) (Huang et al.,
84 2025), likely driven by regional differences in large-scale wind fields and air–sea turbulent heat fluxes (Shen et al.,
85 2024), and potentially modulated by coastline geometry and topographic constraints. Despite recognized impacts
86 of SLB on air quality (Zhao et al., 2022; Wang et al., 2023; Zheng et al., 2024), only a few case studies have
87 examined how SLB-driven recirculation of nocturnally respired CO₂ can perturb daytime coastal CO₂
88 measurements and may bias emission inversions (Ahmadov et al., 2007), and systematic quantification across
89 coastal cities remains limited.

90

91 Urban greening reinforces the need for explicit source–sink separation because neglecting biogenic contributions
92 can bias inferred urban emissions (Miller et al., 2020; Ye et al., 2020; Sargent et al., 2018). Moreover, urban
93 vegetation is often highly fragmented and can be underrepresented in moderate-to-coarse remote-sensing land-
94 cover/canopy products, which may miss fine-scale urban heterogeneity and thereby introduce additional

95 uncertainty (and potential bias) into satellite-driven biogenic flux estimates (Ma et al., 2022; Corro et al., 2025;
96 Glauch et al., 2025). Green coverage within built-up urban areas is similarly high across major Chinese coastal
97 megacities (e.g., Guangzhou: 43.7 % in 2023; Shenzhen: 44.0 % in 2023; Qingdao: 44.0 % in 2023; Tianjin: 38.2 %
98 in 2023) (Guangzhou Municipal Bureau of Statistics, 2024; Shenzhen Municipal Bureau of Statistics, 2024;
99 Qingdao Municipal Bureau of Statistics, 2024; Tianjin Municipal Bureau of Statistics, 2024), implying that
100 biogenic exchange can be non-negligible when interpreting urban observations. For example, in coastal North
101 American cities, high-resolution vegetation modeling in New York City indicates that summertime biogenic uptake
102 can offset up to 40 % of afternoon anthropogenic CO₂ enhancements and can fully balance on-road traffic
103 contributions (Wei et al., 2022), while a dense-sensor analysis in Los Angeles suggests that daytime biogenic
104 exchange can consume up to 60 % of fossil-fuel emissions during the peak growing season (Kim et al., 2025).
105 Recent advances, including emerging atmospheric constraints such as carbonyl sulfide (COS), further demonstrate
106 the feasibility and value of more robust biogenic quantification in city carbon budgets (Soininen et al., 2025).

107

108 Taken together, three knowledge gaps limit the interpretation of coastal megacity CO₂ observations and their use
109 for mitigation assessment: (i) how spatiotemporal CO₂ patterns vary across a coastal–urban–suburban gradient; (ii)
110 how SLB-driven transport and boundary-layer mixing reshape diurnal and seasonal CO₂ signals through seasonally
111 varying ventilation, boundary-layer depth, and atmospheric stability, which may differ from inland-city regimes;
112 and (iii) how fossil-fuel and biogenic contributions can be robustly separated, with quantified uncertainty, in a
113 coastal setting. To bridge these gaps, we investigate Guangzhou (Pearl River Delta, China) as a living laboratory:
114 high GDP and population indicate strong energy and mobility demand and thus substantial fossil-fuel CO₂
115 emissions, while evergreen urban vegetation, a long growing season, and frequent SLB circulation can produce
116 non-negligible biogenic signals and complex coastal transport. The policy context further elevates the value of
117 attribution: Guangdong’s emissions-trading system (ETS) has operated since 2013, alongside measures targeting
118 energy structure, vehicle emissions, building efficiency, and urban greening.

119

120 Given this imperative to track changes in urban emissions and net carbon exchange, we use an observation-driven
121 framework that complements atmospheric inversion approaches and interprets diurnal–seasonal variability by
122 combining multi-site in-situ CO₂ and CO measurements with footprint-informed transport analysis (Lin et al., 2003;
123 Fasoli et al., 2018). Unlike a formal Bayesian 3-D inversion, our framework targets process attribution of observed
124 variability and quantifies robustness through sensitivity tests rather than posterior flux estimates. This approach
125 emphasizes process-level interpretation of concentration variability while explicitly evaluating key uncertainty

126 sources. While CO is widely used to infer fossil-fuel CO₂, it carries inherent uncertainties due to varying emission
127 ratios (R_{CO}), background variability, and atmospheric chemical processing (Turnbull et al., 2011; Chen et al., 2020;
128 Griffin et al., 2007; Vimont et al., 2019). Footprint estimates are likewise sensitive to meteorological forcing and
129 boundary-layer representation, and such transport sensitivities may be amplified under complex coastal mesoscale
130 flows. We therefore quantify uncertainties associated with measurement and background selection, evaluate
131 robustness to transport-model setup via STILT configuration tests, assess biogenic consistency using seasonal
132 vegetation activity (e.g., NDVI), and utilize emission inventories for contextual comparison—using inter-inventory
133 spread as a plausibility envelope for benchmarking rather than a validation target.

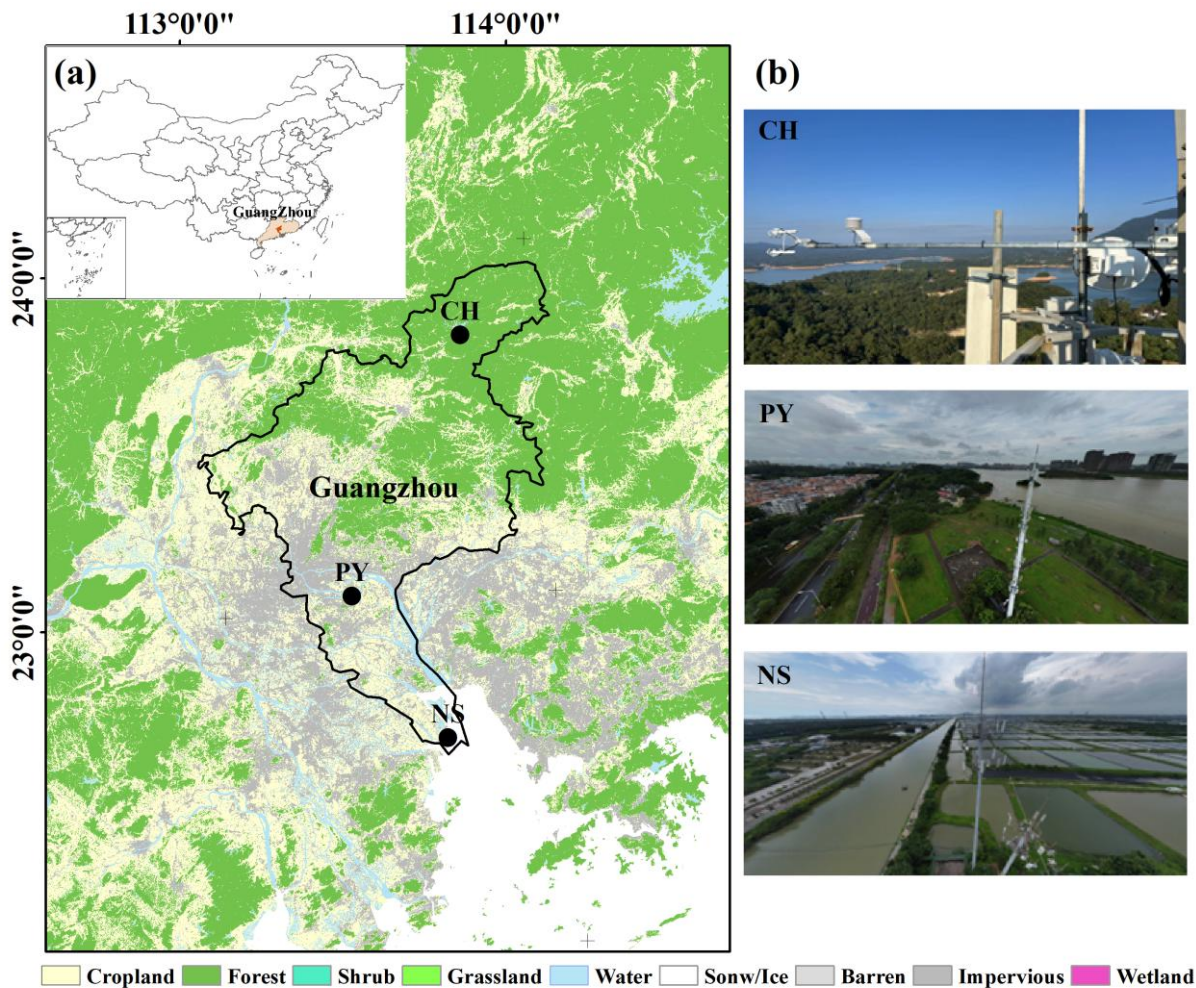
134

135 Accordingly, we aim to: (i) resolve spatiotemporal patterns of CO₂ across three sites spanning near-coastal (NS),
136 urban-core (PY), and suburban (CH) environments; (ii) quantify how SLB modulates diurnal-seasonal CO₂
137 variability and interpret the contrasts in terms of changes in wind ventilation, boundary-layer depth, and seasonally
138 varying atmospheric stability/stratification; and (iii) partition observed CO₂ enhancements at the urban site (PY)
139 into fossil-fuel and biogenic components using CO and footprint information, with explicit uncertainty
140 characterization via measurement/background terms and STILT configuration sensitivity tests.

141 **2 Data and methodology**

142 **2.1 Observational sites**

143 The high-precision greenhouse gas monitoring network in Guangzhou is illustrated in Fig. 1. Three stations—
144 Nansha (NS), Panyu (PY), and Conghua (CH) are symmetrically distributed along the city’s predominant south–
145 north wind axis, representing coastal, urban, and suburban atmospheric conditions, respectively. Site selection
146 criteria are detailed in the Supplement. All stations employ tower-based sampling at similar heights: NS and PY at
147 48 m, and CH at 40 m. Monitoring spanned from January 1, 2023, to September 30, 2024. From PY, the straight-
148 line distances to NS and CH are 54 km and 89 km, respectively.



149

150 **Figure 1.** (a) Geographic locations of the NS, PY, and CH stations, with regional land use classification based on the 30 m
 151 resolution 2023 land cover product of China (CLCD) (Yang and Huang, 2025). (b) Photographs of each station.

152 The NS station (113.63° E, 22.61° N) is located < 5 km from the coastline. This coastal site is surrounded by
 153 aquaculture ponds and sparse wetlands. Infrastructure nearby includes the under-construction southern extension
 154 of Guangzhou Metro Line 18 (NW direction) and the S78 highway (~ 2 km west). The PY station (113.38° E,
 155 23.03° N) is situated in the densely populated urban core; the tower is adjacent to Guangzhou University Town
 156 (north) and the Pearl River (south). A city road (~ 100 m north) and the S73 expressway (~ 700 m west) contribute
 157 to local emissions. The CH station (113.78° E, 23.74° N) is positioned in the northern suburbs. The site is bordered
 158 by subtropical evergreen broadleaf forests (north), a tourist resort (south), and a tea processing plant. The G45
 159 highway lies ~ 3 km northwest. According to the Emissions Database for Global Atmospheric Research (EDGAR)
 160 Community GHG database (EDGAR_2024_GHG; 2023; 0.1° × 0.1°) (Crippa et al., 2024), grid-level CO₂ emission
 161 densities for NS, PY, and CH are 3456, 15244, and 203 ton km⁻² yr⁻¹, respectively (Fig. S1 in the Supplement).

162 2.2 Monitoring system

163 All three stations are equipped with similar monitoring systems, consisting of sampling modules, calibration

164 modules, gas analyzers, and data acquisition systems. Notably, the NS and PY stations utilize Picarro G2401
165 greenhouse gas analyzers to measure CO₂/CH₄/CO/H₂O, with a CO₂ measurement precision of < 20 ppb (5 min, 1
166 σ). The CH station employs an ABB GLA331-GGA greenhouse gas analyzer to measure CO₂/CH₄/H₂O, with a
167 CO₂ measurement precision of < 25 ppb (5 min, 1 σ). N₂O and CO are measured using a GLA351-N2OCM analyzer.
168 Detailed monitoring system and principles of the instruments are provided in the Supplement. Prior to field
169 deployment, comparative tests were conducted in the laboratory to ensure the analytical performance consistency
170 of the instruments. Additionally, meteorological sensors (measuring wind speed, direction, humidity, temperature,
171 and pressure) are installed at the same height as the sampling inlets at NS and PY stations, while the CH station
172 lacks such sensors. Detailed descriptions of wind field characteristics at NS and PY stations are included in the
173 Supplement and illustrated in Fig. S2.

174 **2.3 Calibration methods**

175 The calibration module comprises two components: working standard curve establishment and target gas
176 verification. High- and low-concentration standard gases are used to establish calibration curves, while a mid-
177 concentration standard gas is used for target verification. The target and calibration gases are stored in inert-coated
178 aluminum cylinders, uniformly supplied by the China National Environmental Monitoring Center. All stations
179 follow the same calibration protocol: (1) weekly calibration curve establishment: high- and low-concentration gases
180 are injected for 30 minutes each, with the final 5 minutes of instrument response used for calibration; (2) target gas
181 verification every 12 h: mid-concentration gas is injected for 30 minutes, with the final 5 minutes of response used
182 for verification; (3) re-calibration is triggered if the residual value (H) from target verification exceeds ± 0.2 ppm.
183

184 Calibration curves are derived from the instrument's response to calibration gas, yielding a linear calibration
185 equation:

$$186 \quad Y = A \times X - B, \quad (1)$$

187 where A, B are calibration coefficients. Calibrated CO₂ (CO_{2,k}) is calculated by:

$$188 \quad CO_{2,k} = A \times CO_{2,m} - B, \quad (2)$$

189 where CO_{2,m} is the measured response. Daily 12 h target gas verification is conducted to assess analyzer accuracy
190 and stability by calculating the residual H:

$$191 \quad H = (A \times CO_{2,c} - B) - CO_{2,n} . \quad (3)$$

192 where CO_{2,n} is the standard CO₂ concentration of the target gas, and CO_{2,c} is the analyzer response/reading to the
193 target gas.

194

195 To ensure high-precision and stable monitoring results, periods with $|H| \leq 0.1$ ppm are prioritized. Measurement
196 uncertainties for the analyzers at NS, PY, and CH stations, calculated as the standard deviation (SD) of H (Yang et
197 al., 2021), are 0.04, 0.02, and 0.04 ppm, respectively. In addition to daily calibration, maintenance personnel
198 conduct weekly inspections of instruments and station facilities, including checks on power supply stability, data
199 logger functionality, and industrial control computer status. Consumables (e.g., filters) are replaced as needed, and
200 emergency repairs or instrument overhauls are performed when necessary. Any instrument downtime caused by
201 internal or external factors is documented in maintenance logs, and affected data is flagged. Throughout the
202 monitoring period, all three stations maintained data validity rates exceeding 90 %.

203 **2.4 Sea–land breeze identification**

204 The straight-line distances from the NS, PY, and CH stations to the coastline are 4, 58, and 130 km, respectively.
205 The NS station, closest to the coast, was selected to study Guangzhou’s sea–land breeze (SLB) circulation. Prior to
206 SLB identification, local and background winds must be differentiated, as tower-measured winds (Fig. S2 in the
207 Supplement) represent superimposed local and background wind fields, where strong background winds can
208 obscure SLB signals (Qiu and Fan, 2013). The following equations distinguish background winds from local winds
209 (Sun et al., 2022; Shen et al., 2019):

$$210 \quad U_b = \overline{\sum_{i=0}^{23} U_i}, \quad (4)$$

$$211 \quad V_b = \overline{\sum_{i=0}^{23} V_i}, \quad (5)$$

$$212 \quad U_l = U_o - U_b, \quad (6)$$

$$213 \quad V_l = V_o - V_b. \quad (7)$$

214 where U_o and V_o are the observed wind fields from the tower, U_b and V_b denote background winds, and U_l and V_l
215 represent local winds.

216

217 A sea–land breeze day (SLBD) is defined as any 24 h period exhibiting a distinct transition from sea breezes during
218 the day to land breezes at night (Xiao et al., 2023). SLB identification criteria vary regionally due to differences in
219 topography and coastline geometry (Huang et al., 2025). Guided by the SLB criteria in Supplementary Table S1
220 and historical patterns for the Pearl River Estuary (Qiu and Fan, 2013; Zhang et al., 2024; Mai et al., 2024b), we
221 define for the north-shore site (NS) directional sectors of $112\text{--}202^\circ$ for the sea breeze and $302\text{--}45^\circ$ for the land
222 breeze. The corresponding detection windows are 12:00–20:00 LT (sea breeze) and 01:00–09:00 LT (land breeze),

223 consistent with regional SLB climatologies. Directional persistence is evaluated using the local-wind direction. The
224 wind-speed screen is applied to the observed wind-speed magnitude at 48 m. A day is labeled as an SLB day only
225 if all the following conditions are satisfied: (1) Directional persistence: within each window, the local wind
226 direction (from the decomposed local component) stays inside the corresponding sector for ≥ 4 h, or for ≥ 4 h within
227 any running 5 h window; and (2) Weak-forcing screen: for the same candidate SLB day, the observed wind-speed
228 magnitude at 48 m must remain $< 10 \text{ m s}^{-1}$ at every hour of that day (i.e., no hourly value exceeds 10 m s^{-1}). This
229 conservative cap follows coastal-China SLB climatologies and is intended to exclude strongly forced days (Qiu
230 and Fan, 2013; Sun et al., 2022; Huang et al., 2025; Zhang et al., 2024). Otherwise, the day is designated a non-
231 SLB day (NSLBD).

232

233 Together, these two requirements reduce the likelihood of misclassification under strongly forced conditions. Days
234 dominated by synoptic forcing or tropical-cyclone peripheries often show a prolonged anomalous wind regime
235 rather than a clear diurnal reversal (Atkins and Wakimoto, 1997; Allouche et al., 2023). To explicitly assess residual
236 tropical-cyclone (TC) contamination, we cross-referenced the SLB calendar with 2023 Pearl River Delta
237 (PRD)/Guangzhou TC impact windows compiled from the official Guangdong–Hong Kong–Macao Greater Bay
238 Area (GBA) Climate Monitoring Bulletin (Table S2). For each TC, impact start/end are defined as the first/last
239 local dates on which the bulletin reports PRD/Guangzhou impacts or advisories attributable to that system
240 (including peripheral rainbands/gusts). Because the bulletin is date-based, we conservatively treat the entire day
241 within each window as potentially TC-influenced. Only one SLBD (2 Sep 2023) falls within these windows;
242 excluding it leaves results unchanged.

243 **2.5 Estimation of CO_2^{tot} , CO_2^{ff} , and CO_2^{bio}**

244 The observed CO_2 concentration enhancements at tall-tower receptor sites represent the integrated influence of
245 upwind surface fluxes transported by atmospheric advection and mixing (Lin et al., 2003). Consequently, upwind
246 carbon emissions can be inferred from site-specific enhancement measurements coupled with their corresponding
247 atmospheric footprints. Here we apply an observation-driven framework that combines concentration-enhancement
248 observations with transport-model footprints to estimate total CO_2 (CO_2^{tot}) and CO (CO^{tot}) surface fluxes, and to
249 further derive fossil-fuel (CO_2^{ff}) and biogenic (CO_2^{bio}) components using the site-specific $\Delta\text{CO}/\Delta\text{CO}_2$ relationship
250 (R_{CO}), without relying on any a priori emissions inventory. The required inputs are limited to enhancement
251 observations at the receptor sites and atmospheric footprints, consistent with previous regional flux quantifications
252 for CO_2 , CH_4 , and CO (Mitchell et al., 2018; Lin et al., 2021; Wu et al., 2022a). Emission inventories are used only

253 for site-context characterization (Sect. 2.1) and, subsequently, for an independent bottom-up plausibility envelope
 254 for winter-afternoon flux estimates (Sect. 3.5), rather than as priors or validation targets. CO_{2tot} and CO_{tot} are
 255 calculated as:

$$256 \quad CO_{2tot} = \frac{CO_{2,s}obs - CO_{2}bg}{\sum_i Footprint_{i,s}}, \quad (8)$$

$$257 \quad CO_{tot} = \frac{CO_sobs - CObg}{\sum_i Footprint_{i,s}}, \quad (9)$$

258 The numerators are hourly CO_2 and CO concentration enhancements (ΔCO_2 and ΔCO) at station s , where $CO_{2,s}obs$
 259 and CO_sobs represent observed CO_2 and CO concentrations, while $CO_{2}bg$ and $CObg$ denote urban background
 260 concentrations (detailed in the Supplement). The denominators are hourly total atmospheric footprints
 261 ($\sum_i Footprint_{i,s}$), where i denotes backward particle release time from the receptor. Due to challenges in modeling
 262 mixed-layer depths during nighttime, morning, and evening, flux analysis focuses on afternoon hours (12:00–16:00)
 263 (Boon et al., 2016; Mitchell et al., 2018; Lin et al., 2021). Daily-scale CO_{2tot} and CO_{tot} are derived by dividing
 264 the mean afternoon ΔCO_2 and ΔCO by the corresponding mean $\sum_i Footprint_{i,s}$. The footprint quantifies the
 265 sensitivity of concentration enhancements at the observation site to upwind surface fluxes, as detailed in Sect. 2.5.1.
 266 ΔCO_2 is in units of [ppm], while footprint is in [ppm / ($\mu mol m^{-2} s^{-1}$)], so CO_{2tot} , the quotient between the two
 267 quantities, is in flux units of [$\mu mol m^{-2} s^{-1}$].

268

269 Anthropogenic CO_2 emissions (CO_{2ff}) are derived from CO_{tot} and the CO/ CO_2 emission ratio (R_{CO}), where R_{CO} is
 270 determined from real-time tower-measured data, as described in detail in Sect. 3.4:

$$271 \quad CO_{2ff} = \frac{CO_{tot}}{R_{CO}}, \quad (10)$$

272 Biogenic fluxes (CO_{2bio}) are calculated as residuals:

$$273 \quad CO_{2bio} = CO_{2tot} - CO_{2ff}. \quad (11)$$

274 Positive CO_{2bio} values indicate biogenic carbon emissions, while negative values denote carbon uptake, reflecting
 275 the dual role of urban biospheres as CO_2 sources and sinks (Kim et al., 2025).

276 **2.5.1 Atmospheric transport model**

277 To trace air mass sources entering the urban domain and reaching observation sites, and to assess CO_2 emissions
 278 corresponding to observed concentration enhancements, the Stochastic Time-Inverted Lagrangian Transport model
 279 (STILT-Rv2) was employed for atmospheric transport simulations, driven by meteorological fields from the
 280 Weather Research and Forecasting Model (WRFv4.1.1). In this study, STILT serves two purposes: (1) providing

281 airmass trajectories for identifying marine background concentrations in Guangzhou, and (2) generating
282 atmospheric footprints for quantifying total CO₂ and CO emissions.

283

284 The STILT model simulates atmospheric transport by releasing a set of air particles backward in time from the
285 receptor location at the observation height. These particles are tracked spatially and temporally as they disperse
286 upwind. The resulting trajectories delineate source regions influencing the receptor site and quantify the sensitivity
287 of observed concentrations to upwind surface fluxes, termed "source–receptor relationships" or "atmospheric
288 footprints" (Lin et al., 2003; Fasoli et al., 2018). Footprints represent the contribution of upwind sources/sinks to
289 downwind concentration changes, with higher sensitivities near receptors or under stable wind conditions, where
290 boundary layer airmasses interact more directly with surface fluxes (Wu et al., 2022a). For this study, 500 particles
291 were released at 48 m (PY station) heights, and traced backwards in time for 72 h. Footprints were computed at
292 0.08° × 0.08° spatial resolution. Periods with total footprint sensitivities ($\sum_i \text{Footprint}_i$) below the 10th percentile
293 were excluded, indicating low sensitivity to regional surface fluxes (Lin et al., 2021).

294

295 To evaluate whether STILT setup choices could bias the inferred fluxes, we performed targeted wintertime
296 sensitivity experiments at PY using paired daily comparisons (n = 18). Starting from the baseline (500 particles,
297 0.08° grid, 72 h backward), we independently varied (1) particle number (1000, 2000), (2) grid resolution (0.05°,
298 0.10°), and (3) backward duration (96 h, 120 h). For each variant we recomputed footprints, reran the flux-
299 estimation framework, and compared paired daily afternoon means (12:00–16:00 LT) of CO₂tot, CO₂ff and CO₂bio
300 to the baseline using percent differences, Pearson r, and paired t-tests. Percent differences quantify effect size,
301 Pearson r assesses day-to-day consistency, and paired t-tests evaluate detectability of systematic mean shifts. This
302 paired-day design isolates transport-model parameter effects from day-to-day meteorology and observation
303 sampling.

304 **2.5.2 Uncertainty sources**

305 Uncertainties associated with the emission estimates inferred from Eqs. (12)–(14) primarily arise from four sources:
306 (1) observational uncertainty, (2) background concentration uncertainty, (3) atmospheric transport (footprint)
307 uncertainty, and (4) R_{CO}-related uncertainty. We do not explicitly propagate transport/footprint uncertainty within
308 the analytical error propagation of Eqs. (12)–(14); instead, we evaluate sensitivity to transport-model setup using a
309 winter paired-day STILT sensitivity analysis (Sect. 2.5.1; Sect. 3.5; Fig. 11). Residual transport biases (e.g., winds
310 and boundary-layer mixing) remain unquantified and may bias the inferred fluxes, thereby contributing to

311 inventory–observation differences when benchmarking against independent bottom-up inventories, alongside
 312 emission-inventory uncertainty and the representativeness mismatch between footprint-weighted enhancements
 313 and unweighted inventory means (discussed further in Sect. 3.5). Uncertainty associated with R_{CO} is not explicitly
 314 propagated as a formal regression-parameter uncertainty in this study; because R_{CO} is derived from CO and CO₂
 315 enhancements, its uncertainty is expected to be driven mainly by uncertainties in the underlying enhancements
 316 (items 1–2) and scatter in the site-specific relationship. Among the quantified terms, uncertainties in CO₂tot are
 317 dominated by observational and background concentration errors. Uncertainties in CO₂ff are additionally affected
 318 by R_{CO} -related variability, while uncertainties in CO₂bio and the CO₂bio/CO₂ff offset ratio are propagated from
 319 CO₂tot and CO₂ff. Accordingly, the combined uncertainty term is calculated as:

$$320 \quad E_u^2 = OBS_{u,c}^2 + BG_u^2, \quad (12)$$

321 where $OBS_{u,c}$ represents uncertainty in urban atmospheric observations, and BG_u represents uncertainty in urban
 322 background concentrations. We cannot accurately quantify all error sources involved in instrumental measurements;
 323 some minor error sources (e.g., uncertainty related to water vapor) may be negligible, while the primary uncertainty
 324 originates from discrepancies between measured concentrations and calibration standards (Verhulst et al., 2017).
 325 Here, $OBS_{u,c}$ is calculated as the standard deviation (SD) of residuals H (Yang et al., 2021). For urban background
 326 uncertainties:

$$327 \quad BG_{u,co2}^2 = CT_{co2,r}^2 + CT_{co2,s}^2, \quad (13)$$

$$328 \quad BG_{u,co}^2 = OBS_{co,r}^2 + OBS_{co,s}^2. \quad (14)$$

329 CO₂ background uncertainty ($BG_{u,co2}$) combines the absolute monthly smoothed residuals ($CT_{co2,r}$) and variability
 330 (SD) of monthly CO₂ concentrations ($CT_{co2,s}$) from CarbonTracker (CT). Similarly, CO background
 331 uncertainty ($BG_{u,co}$) is derived from monthly smoothed residuals ($OBS_{co,r}$) and variability ($OBS_{co,s}$) of in situ
 332 observations.

333

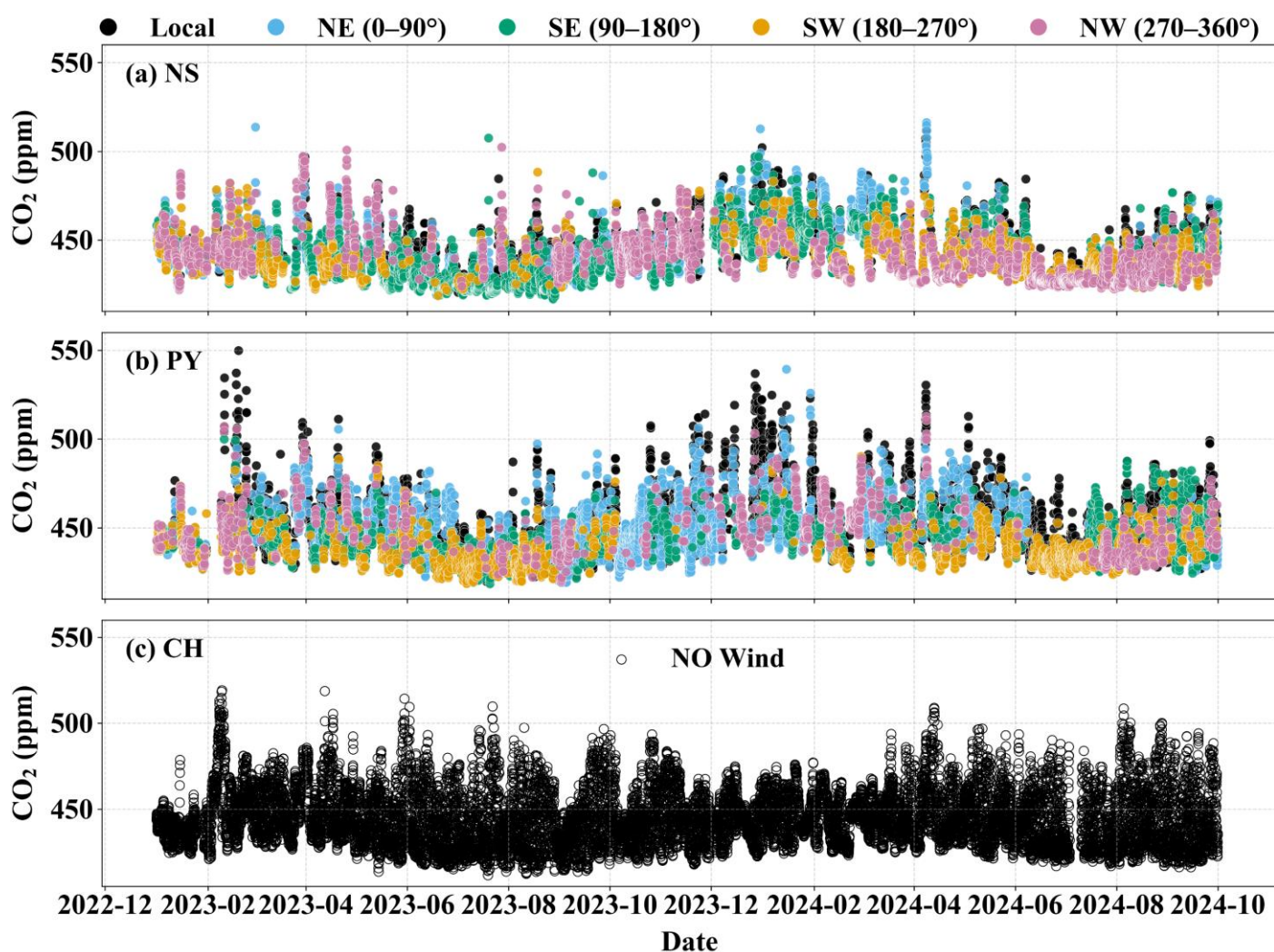
334 To guard against bias from transport settings, the paired-day sensitivity analysis is conducted relative to the baseline;
 335 we treat effect sizes and 95 % confidence intervals (CIs) as primary quantities and report p-values only to indicate
 336 detectability given $n = 18$, with quantitative outcomes presented in Sect. 3.5 and Fig. 11.

337 **3 Results and discussion**

338 **3.1 Spatiotemporal patterns of atmospheric CO₂**

339 Figure 2 presents the hourly mean time series of atmospheric CO₂ concentrations at the NS, PY, and CH stations

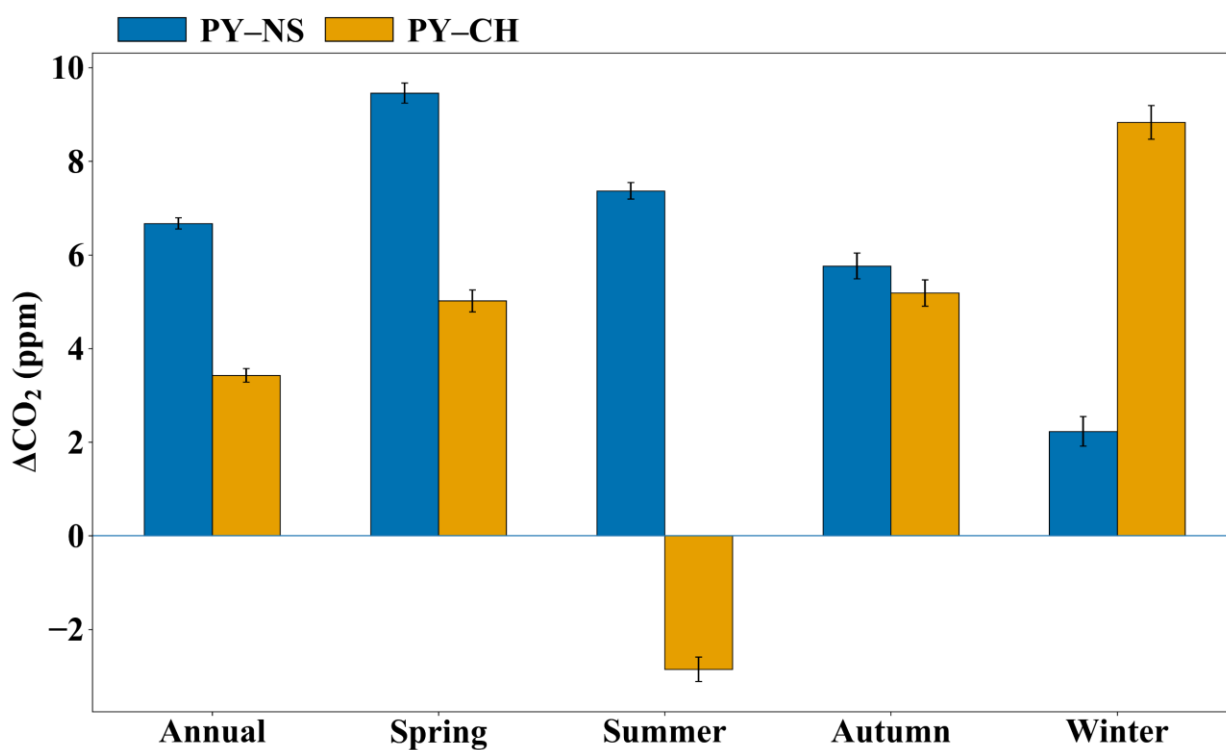
340 in Guangzhou from January 1, 2023, to September 30, 2024. To assess wind field impacts on CO₂ variability (Fig.
 341 S2), concentrations were classified into five categories: local (wind speed < 1.5 m s⁻¹) and four directional sectors
 342 (wind speed ≥ 1.5 m s⁻¹) defined as NE (0–90°), SE (90–180°), SW (180–270°), and NW (270–360°). All stations
 343 exhibited significant temporal variability, with standard deviations (SD) of 13.90 (NS), 15.92 (PY), and 16.05 ppm
 344 (CH), consistent with urban and suburban observations in Hangzhou, Beijing, Xi'an, and Seoul (Park et al., 2021;
 345 Yang et al., 2021; Chen et al., 2024; Liu et al., 2025). PY showed the highest CO₂ levels and variability, driven
 346 predominantly by local-type emissions under low wind speeds. In contrast, the NS coastal station exhibited
 347 elevated concentrations during northerly winds (NW/NE). Seasonal wind effects were pronounced:
 348 summer southerly winds (SW/SE) generally reduced CO₂ at PY and NS (most notably at NS near the coast), while
 349 winter northerly winds (NW/NE) often increased CO₂ at NS.



350

351 **Figure 2.** Time series of atmospheric CO₂ concentrations at the (a) NS, (b) PY, and (c) CH stations, points are color-
 352 coded by wind category: local conditions (wind speed < 1.5 m s⁻¹) and four directional sectors for winds ≥ 1.5 m s⁻¹ (NE, 0–
 353 90°; SE, 90–180°; SW, 180–270°; NW, 270–360°). For CH, wind-direction classification is not shown and the time series is
 354 plotted without sector coloring.

355 Urban–rural CO₂ gradients vary globally due to differences in economic activity, population density, land use, and
 356 energy infrastructure, reflecting heterogeneous urban carbon emissions (Gao et al., 2022). To further illustrate this
 357 spatial contrast and its seasonality, we summarized the urban–suburban/coastal gradients across the full record and
 358 report annual and seasonal means in Fig. 3. In Guangzhou, mean CO₂ concentration differences between PY and
 359 NS/CH were 6.67 and 3.43 ppm, respectively, forming a distinct "urban dome" (urban > suburban > coastal). The
 360 NS–CH difference (3.44 ppm) highlights comparable gradients between suburban and coastal zones. This gradient
 361 mirrors Los Angeles’s coastal megacity profile but with a smaller magnitude (Verhulst et al., 2017). Guangzhou’s
 362 urban–suburban difference (3.43 ppm) aligns with Hangzhou’s 2021 observations (4.96 ppm) (Chen et al., 2024)
 363 but is lower than Nanjing (8.1 ppm, 2014) and Beijing (12.4 ppm, 2018–2019) (Gao et al., 2018; Yang et al., 2021).
 364 It remains far smaller than Shanghai (55.1 ppm, 2014) and Baltimore (66.0 ppm, 2002–2006) (Pan et al., 2016;
 365 George et al., 2007). Over time, urban emissions may stabilize as suburban populations and fossil fuel demand
 366 grow, potentially narrowing urban–suburban CO₂ differences (Mitchell et al., 2018). For instance, Hangzhou’s
 367 reduced gradient reflects urbanization-driven energy consumption, where suburban monitoring captures urban
 368 emission influences (Chen et al., 2024).



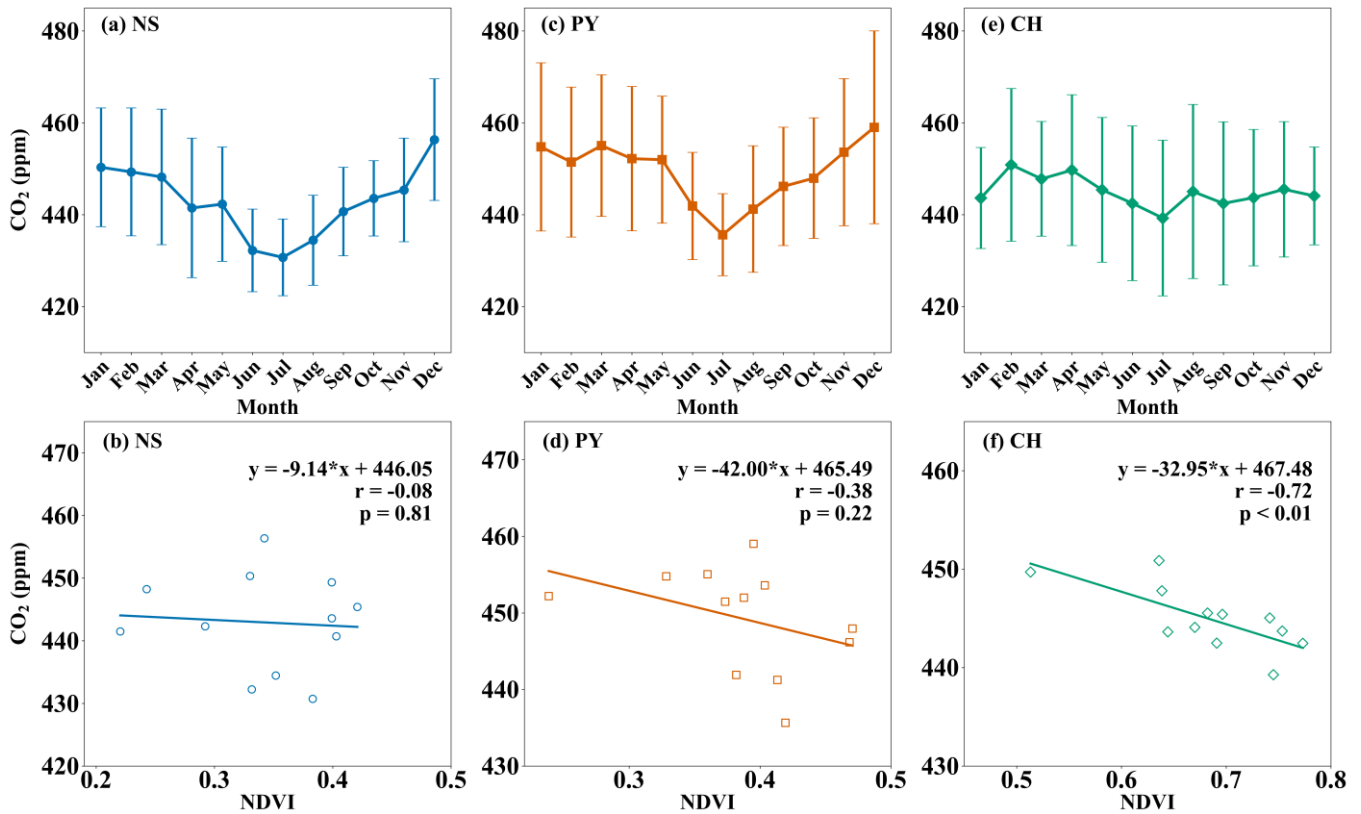
369
 370 **Figure 3.** Urban–suburban/coastal CO₂ gradients in Guangzhou. Annual and seasonal mean concentration differences
 371 (ΔCO_2 , ppm) between the urban site (PY) and the coastal site (NS) (PY–NS) and between PY and the suburban site (CH)
 372 (PY–CH). Seasons are defined as spring (Mar–May), summer (Jun–Aug), autumn (Sep–Nov), and winter (Dec–Feb). Error
 373 bars denote ± 1 standard error (SE).

374 Figure 3 further shows that these spatial gradients are strongly season-dependent. PY–NS remains positive year-

375 round but is smallest in winter (2.23 ppm), when prevailing northerlies elevate CO₂ at the coastal NS site and reduce
376 the urban–coastal contrast, consistent with Fig. 2. PY–CH is more strongly seasonally modulated: it peaks in winter
377 (8.83 ppm) but reverses sign in summer (–2.86 ppm), when southerly (marine-influenced) flow more frequently
378 ventilates PY (SW/SE sectors in Fig. 2) and the CH summertime enhancement may reflect a northward-displaced
379 urban influence plus biogenic/boundary-layer modulation (Sect. 3.1.1; Sect. 3.3). Spring and autumn show
380 intermediate positive PY–CH (~ 5 ppm), while PY–NS peaks in spring (9.46 ppm), consistent with enhanced
381 coastal ventilation under southerly influence. Together, these gradients indicate a seasonally displaced CO₂ “dome”
382 in this coastal setting, where the highest CO₂ within our network can occur outside the urban core, complementing
383 the site-level seasonal cycles discussed in Sect. 3.1.1. This coastal, seasonally displaced CO₂ dome contrasts with
384 patterns more commonly reported in inland megacity networks, where enhancements are typically strongest at the
385 most urbanized sites relative to suburban/background stations (Xueref-Remy et al., 2018; Yang et al., 2021; Chen
386 et al., 2024).

387 **3.1.1 Seasonal variability of atmospheric CO₂**

388 Figure 4 illustrates the monthly mean variations in atmospheric CO₂ concentrations at the NS, PY, and CH stations
389 in Guangzhou, alongside their correlations with the Normalized Difference Vegetation Index (NDVI). NDVI data
390 at 1 km × 1 km spatial resolution were obtained from NASA’s EOSDIS Land Processes Distributed Active Archive
391 Center (Didan, 2015), with values within a 3 km radius buffer around each station center used for comparative
392 analysis. All three stations exhibited consistent seasonal CO₂ patterns, with higher concentrations in winter/spring
393 and lower values in summer/autumn, mirroring observations in Hangzhou (Chen et al., 2024). These variations
394 arise from the combined effects of (1) seasonal biogenic flux cycles, (2) anthropogenic emission variability, and (3)
395 boundary layer height dynamics (Xueref-Remy et al., 2018). Enhanced vegetation photosynthesis during warmer
396 months (summer/autumn, Table S3 in the Supplement) strengthens biogenic carbon sinks, while higher boundary
397 layer depths (Fig. S6 in the Supplement) and southerly marine air masses (Fig. 2) promote atmospheric mixing and
398 CO₂ dispersion.



399

400 **Figure 4.** Monthly mean CO₂ concentrations (upper panels) and their correlations with the Normalized Difference
 401 Vegetation Index (NDVI) (lower panels) for the (a–b) NS, (c–d) PY, and (e–f) CH stations. Error bars indicate ± 1 standard
 402 deviation (SD).

403 The amplitudes of the seasonal variation of CO₂ at NS, PY, and CH are 25.63, 23.38, and 11.59 ppm, respectively.
 404 NS and PY peaked in December and troughed in July, whereas CH peaked in February and troughed in July. NS’s
 405 large amplitude reflects its extreme December highs and July lows. In December, prevailing northerly winds (Figs.
 406 2a and S2a) transported urban emissions to downwind NS, narrowing its CO₂ difference with PY to 2.68 ppm.
 407 Conversely, July saw NS’s CO₂ concentrations fall to the lowest among all stations—4.93 ppm and 8.56 ppm below
 408 PY and CH, respectively—establishing a south-to-north increasing gradient (coastal < urban < suburban). This
 409 gradient aligns with marine-influenced southerly air masses, which dilute coastal CO₂ while transporting urban
 410 emissions northward, potentially accumulating CO₂ in northern suburbs. This south–north pattern is consistent with
 411 the seasonal mean gradients in Fig. 3, which summarize how the urban–coastal contrast weakens in winter and how
 412 the urban–suburban gradient can be seasonally displaced in summer.

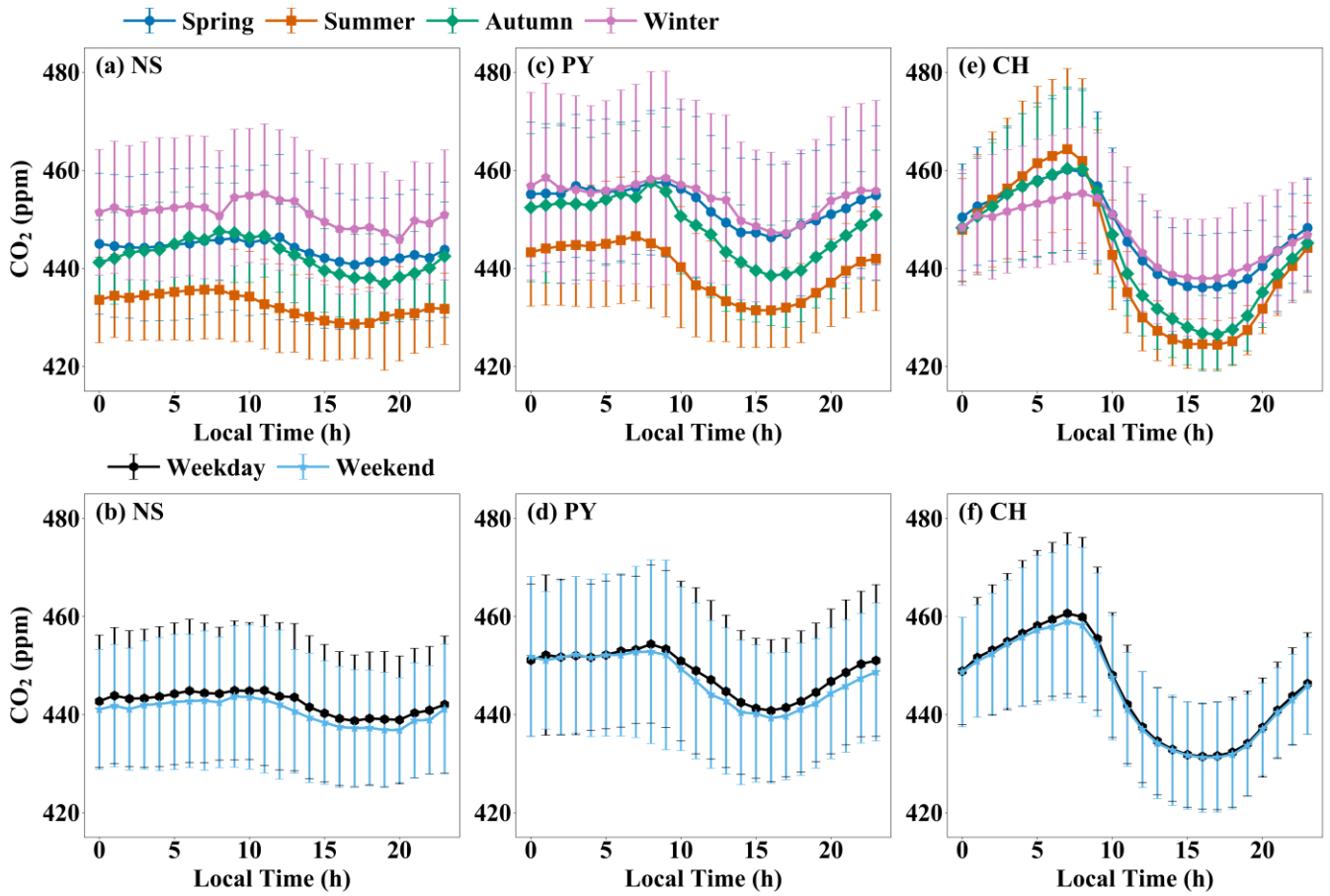
413

414 Although CH exhibits strong biogenic coupling (NDVI–CO₂ correlation: –0.72; Fig. 4f), NS shows an opposite
 415 seasonal contrast relative to CH (–9.80 ppm in summer; +5.80 ppm in winter), pointing to transport- and boundary-
 416 layer-driven variability at the coastal site. At NS, the NDVI–CO₂ correlation is weak (–0.08) and NDVI varies
 417 within a narrow range (0.22–0.42), indicating limited local biogenic control, whereas seasonal shifts in marine–

418 continental transport (summer dilution vs. winter urban outflow) and boundary-layer depth jointly modulate
419 dilution and accumulation (Figs. 2 and S6). In February, CH recorded its annual CO₂ maximum, driven by
420 vegetation respiration during early growth stages and elevated emissions from fireworks around the Lunar New
421 Year, as CH's location falls outside Guangzhou's fireworks restriction zones
422 (https://www.gz.gov.cn/gfxwj/qjgfxwj/chq/qf/content/post_7198980.html, last access: 18 June 2025). This
423 interpretation is supported by CO, a tracer for combustion-derived CO₂ (Newman et al., 2013; Che et al., 2022a):
424 CH's CO concentrations also peaked in February due to firework emissions, whereas other sites peaked in
425 December (Fig. S7 in the Supplement).

426 **3.1.2 Diurnal variations of atmospheric CO₂**

427 The diurnal patterns of atmospheric CO₂ concentrations at NS, PY, and CH stations in Guangzhou consistently
428 exhibited lower daytime and higher nighttime values (Fig. 5). This is attributed to the shallow nocturnal boundary
429 layer, which traps anthropogenic and biogenic fluxes near the surface, elevating CO₂ levels. After sunrise, surface
430 heating deepens the boundary layer, diluting surface emissions and entraining free tropospheric air with lower CO₂
431 concentrations. Concurrently, daytime photosynthetic uptake further reduces near-surface CO₂ (Mitchell et al.,
432 2018). We further evaluate urban–suburban–coastal differences in these processes. At PY, the CO₂ peak occurred
433 at 08:00–09:00, aligning with morning traffic peaks, reflecting dominant anthropogenic influences. CH's peak
434 appeared 1–2 h earlier than PY due to its longitudinal and elevational position, where earlier sunrise accelerates the
435 breakup of the nocturnal stable boundary layer. Both PY and CH reached minima at 16:00–17:00, likely linked to
436 afternoon photosynthetic activity. NS exhibited irregular peak/valley timing.



437
 438 **Figure 5.** Diurnal CO₂ variations at the (a–b) NS, (c–d) PY, and (e–f) CH stations, shown across seasons (upper panels)
 439 and weekdays/weekends (lower panels). Seasons are defined as spring (Mar–May), summer (Jun–Aug), autumn (Sep–Nov),
 440 and winter (Dec–Feb). Error bars indicate ± 1 SD. The corresponding CO diurnal cycles are shown in Fig. S9.

441 Diurnal amplitudes at CH and PY were larger in summer/autumn than winter/spring, driven by vegetation activity
 442 and boundary layer dynamics (Fig. S8 in the Supplement). Summer/autumn conditions in Guangzhou—abundant
 443 light, warmth, and rainfall—optimize vegetation growth, enhancing daytime photosynthesis and nighttime
 444 respiration (Dusenge et al., 2019). Optimal canopy temperatures for subtropical evergreen forests (~ 30 °C) (Liu
 445 et al., 2015) align with CH/PY’s summer/autumn daytime temperatures (Table S3), explaining their amplified
 446 amplitudes. However, the diurnal amplitude of CO₂ at CH in summer and autumn is 2.63 times and 1.77 times that
 447 at PY, respectively. The diurnal amplitude of atmospheric CO₂ concentration at CH in summer is 39.90 ppm, which
 448 is close to the diurnal amplitude of CO₂ concentration in the suburbs of Hangzhou in summer (35.29 ppm) (Chen
 449 et al., 2024). Despite similar temperatures, CH’s larger NDVI range and stronger NDVI–CO₂ correlation (–0.72 vs.
 450 PY; Figs. 4d and f) highlight greater biogenic dominance, with pronounced daytime uptake and nighttime
 451 respiration. NS showed the smallest diurnal amplitudes across seasons (e.g., 5.60 ppm in summer), attributable to
 452 sparse vegetation (low NDVI: 0.22–0.42) and frequent summer southerly marine air masses, which dilute coastal
 453 CO₂.

454

455 Figure 5 contrasts weekday–weekend diurnal CO₂ patterns. All stations generally showed higher weekday
456 concentrations, diverging from Hangzhou and Beijing (Yang et al., 2021; Chen et al., 2024) but aligning with Paris
457 and Boston (Briber et al., 2013; Xueref-Remy et al., 2018). At CH, the daytime weekday–weekend contrast is small.
458 This could reflect a weak anthropogenic weekday–weekend signal relative to other sources of variability, but it
459 does not uniquely diagnose source dominance because transport and boundary-layer mixing may dilute or mask
460 weekday–weekend differences. At PY, the clearer daytime weekend decrease is consistent with reduced on-road
461 activity in the urban core. At NS, weekday CO₂ remains higher across much of the day, which may reflect weekday-
462 intensified construction and port-related logistics in the surrounding area (for example, the Metro Line 18 extension
463 and operations near the Nansha Container Terminal Phase III, ~ 5 km east), superimposed on transport and mixing
464 effects.

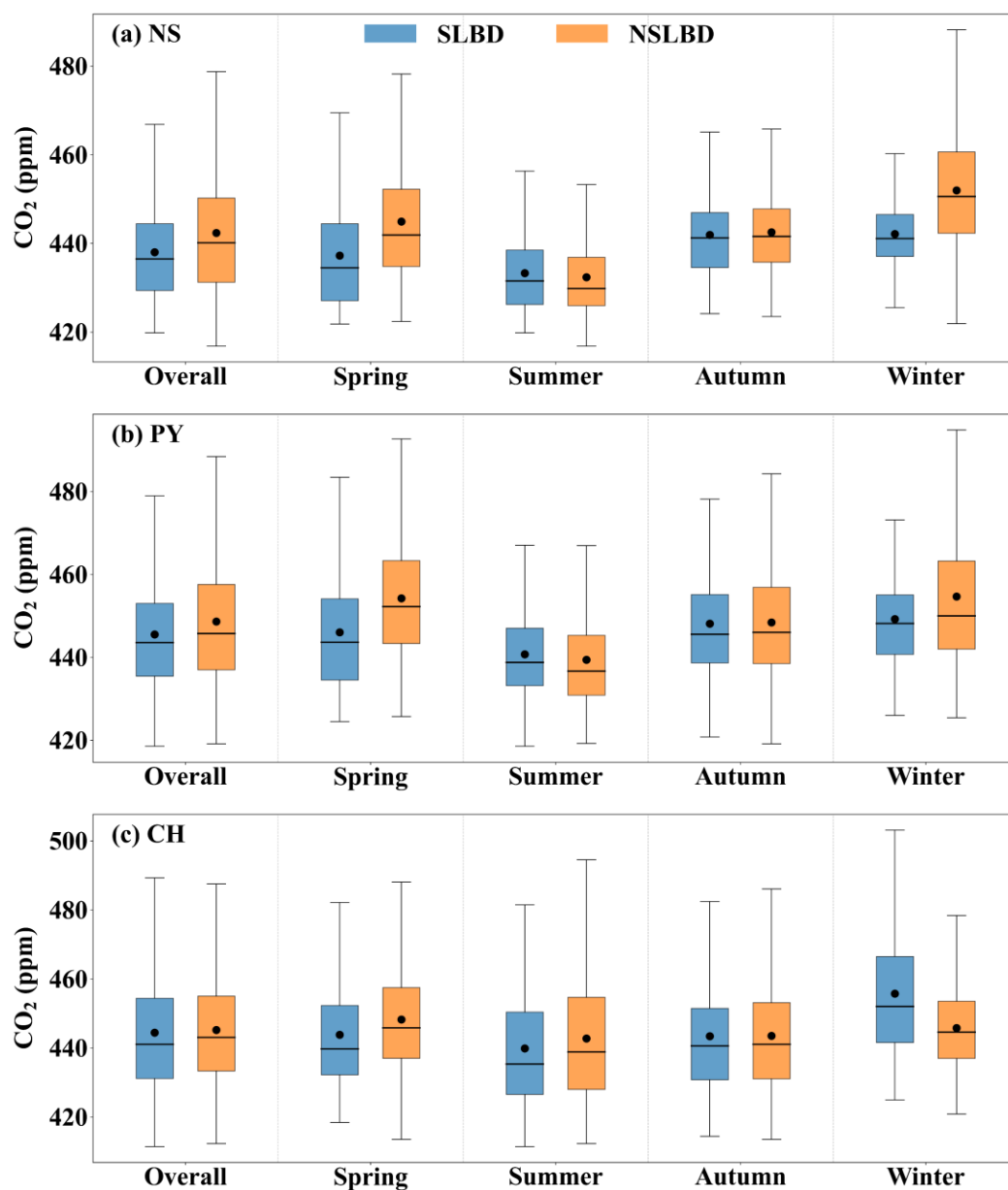
465

466 To corroborate the combustion contribution to the CO₂ diurnal cycle, we examined synchronous CO measurements
467 (Fig. S9 in the Supplement). At all sites, CO shows a consistent seasonal ordering (winter highest, summer lowest),
468 and its morning maximum at PY (typically 08:00–10:00) coincides with the CO₂ morning peak (Fig. 5), supporting
469 traffic/combustion control of the early-day enhancement. In contrast to CO₂, CO exhibits only a weak mid-
470 afternoon minimum (including at CH), consistent with CO₂ being additionally depressed by photosynthetic uptake
471 while CO is unaffected; both species remain modulated by transport and boundary-layer mixing. Weekday–
472 weekend differences are small at CH but clearer at PY/NS (Fig. S9), indicating a stronger anthropogenic weekly-
473 cycle imprint in the urban-core and coastal/port settings. Overall, the CO–CO₂ contrast reinforces our interpretation
474 that the morning CO₂ maxima are primarily combustion-driven, whereas the pronounced mid-afternoon CO₂
475 minima at vegetated sites reflect biogenic uptake rather than reduced emissions.

476 **3.2 Sea–land breeze impacts**

477 Based on meteorological observations from the NS coastal tall tower, 84 sea–land breeze days (SLBD) were
478 identified in Guangzhou between January 2023 and September 2024, accounting for 13.14 % of the monitoring
479 period, with peaks in spring and autumn. These transitional seasons between summer and winter are characterized
480 by weaker synoptic systems and lighter background winds, favoring SLBD occurrence (Mai et al., 2024b). Our
481 results align with SLBD seasonal distributions for the Pearl River Estuary cities of Zhuhai and Guangzhou in 2022
482 (Zhang et al., 2024; Mai et al., 2024b). Figure 6 compares CO₂ concentrations during SLBD and non-SLB days
483 (NSLBD) across stations. Overall, average CO₂ concentrations during SLBD were lower than during NSLBD by
484 5.87 ppm at NS, 3.08 ppm at PY, and 0.75 ppm at CH. This indicates that SLB circulation enhances ventilation and

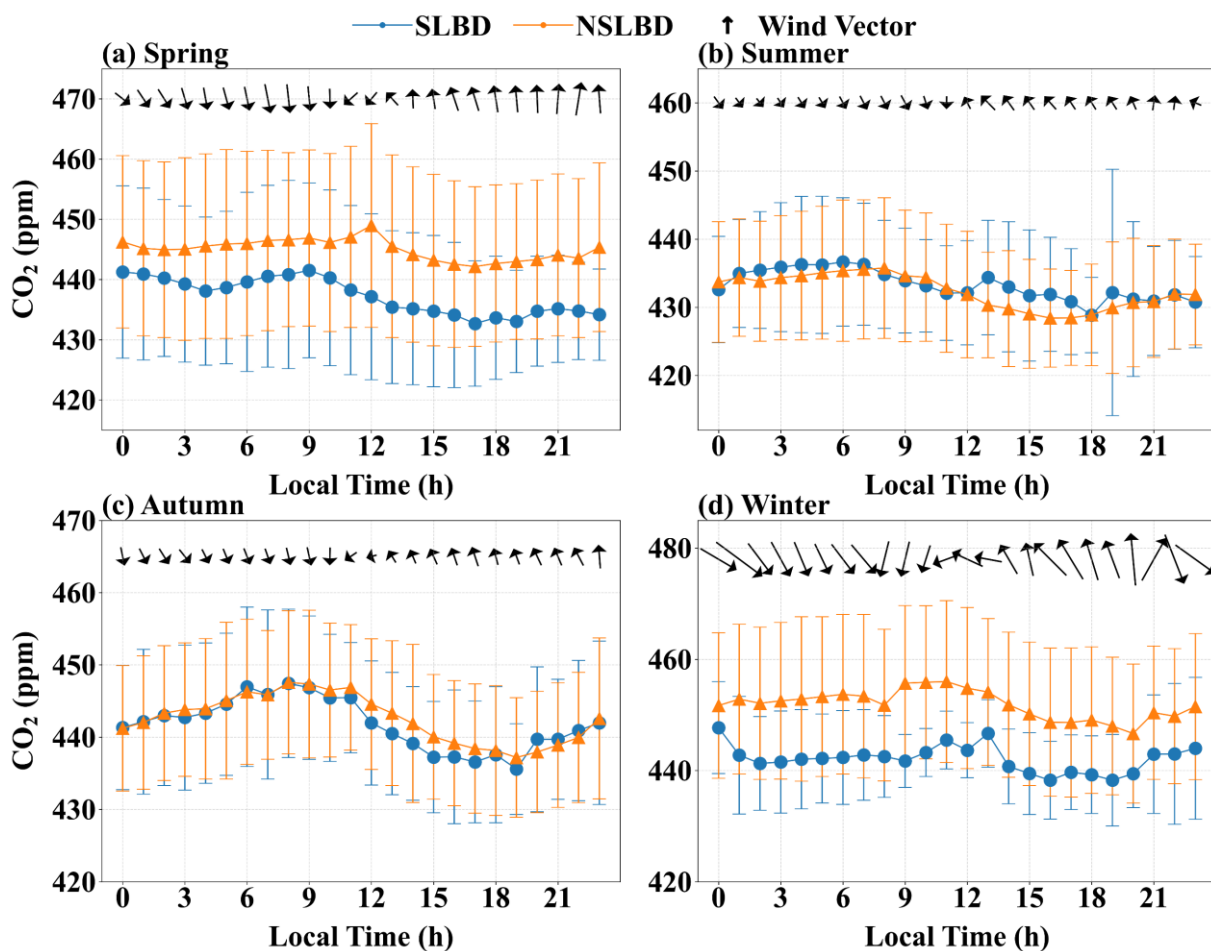
485 CO₂ dispersion, with the SLBD-related reduction decreasing from the coastal site to the urban core and being
 486 smallest at the suburban site (NS > PY > CH). This pattern is similar to SLB-driven dispersion reported for PM_{2.5},
 487 PM₁₀, and ozone in Tianjin (Hao et al., 2017). Seasonal differences were pronounced: SLB promoted CO₂
 488 dispersion at NS and PY in spring, winter, and autumn (spring > winter > autumn), but increased CO₂ accumulation
 489 in summer. Tianjin similarly observed summer PM_{2.5}/PM₁₀ accumulation under SLB (Hao et al., 2017). At CH,
 490 SLBD reduced CO₂ in spring, summer, and autumn but increased it in winter, likely due to limited inland SLB
 491 penetration and competing winter processes.



492
 493 **Figure 6.** Boxplots of atmospheric CO₂ concentrations (black dots denote means; black lines denote medians) during
 494 sea–land breeze days (SLBD) and non-SLB days (NSLBD) across seasons (including overall) for the (a) NS, (b) PY, and (c)
 495 CH stations, with outliers excluded.

496 To resolve seasonal and diurnal SLB impacts, we analyzed CO₂ diurnal variations during SLBD and NSLBD (Fig.

497 7). Focusing on NS (due to similar PY–NS trends and space constraints), spring and winter SLBD reduced CO₂
 498 concentrations by 7.76 ppm and 9.77 ppm (hourly mean differences), respectively, driven by stronger winds (Fig.
 499 7) and deeper boundary layers (Fig. S10 in the Supplement). Autumn SLB only reduced CO₂ during sea breeze
 500 hours (mean difference: 1.69 ppm). Autumn’s weaker winds and boundary layers resulted in reduced dispersion
 501 compared to spring/winter. In summer, SLB increased CO₂ by 2.08 ppm (sea breeze hours) due to stable
 502 atmospheric stratification. Summer temperatures were 6.00 °C and 12.19 °C higher than spring and winter (Table
 503 S3), respectively. Under calm, rain-free conditions, the collision of moist marine air with dry-hot coastal land
 504 formed a thermal internal boundary layer (TIBL), inducing low-level temperature inversions near the SLB
 505 convergence zone (Liu et al., 2001; Reddy et al., 2021). These inversions suppressed horizontal/vertical mixing,
 506 trapping CO₂ (Stauffer et al., 2015; Hao et al., 2024). NS’s summer SLBD winds averaged 1.05 m s⁻¹ (sea breeze)
 507 and 0.96 m s⁻¹ (land breeze)—38.60 %, 63.16 %, and 15.32 % lower than spring, winter, and autumn winds,
 508 respectively—while boundary layer heights (590.54 m) were 9.51 % shallower than NSLBD (Fig. S10). Weak
 509 winds and shallow boundary layers stabilized atmospheric stratification, limiting CO₂ dispersion and elevating
 510 ground-level CO₂ by up to 4.03 ppm.



511

512

Figure 7. Diurnal variations in CO₂ concentrations, wind direction, and wind speed at the coastal station (NS) during

513 sea–land breeze days (SLBD) and non-SLB days (NSLBD) for (a) spring (Mar–May), (b) summer (Jun–Aug), (c) autumn
514 (Sep–Nov), and (d) winter (Dec–Feb). Error bars indicate ± 1 SD. The corresponding CO diurnal cycles are shown in Fig.
515 S11.

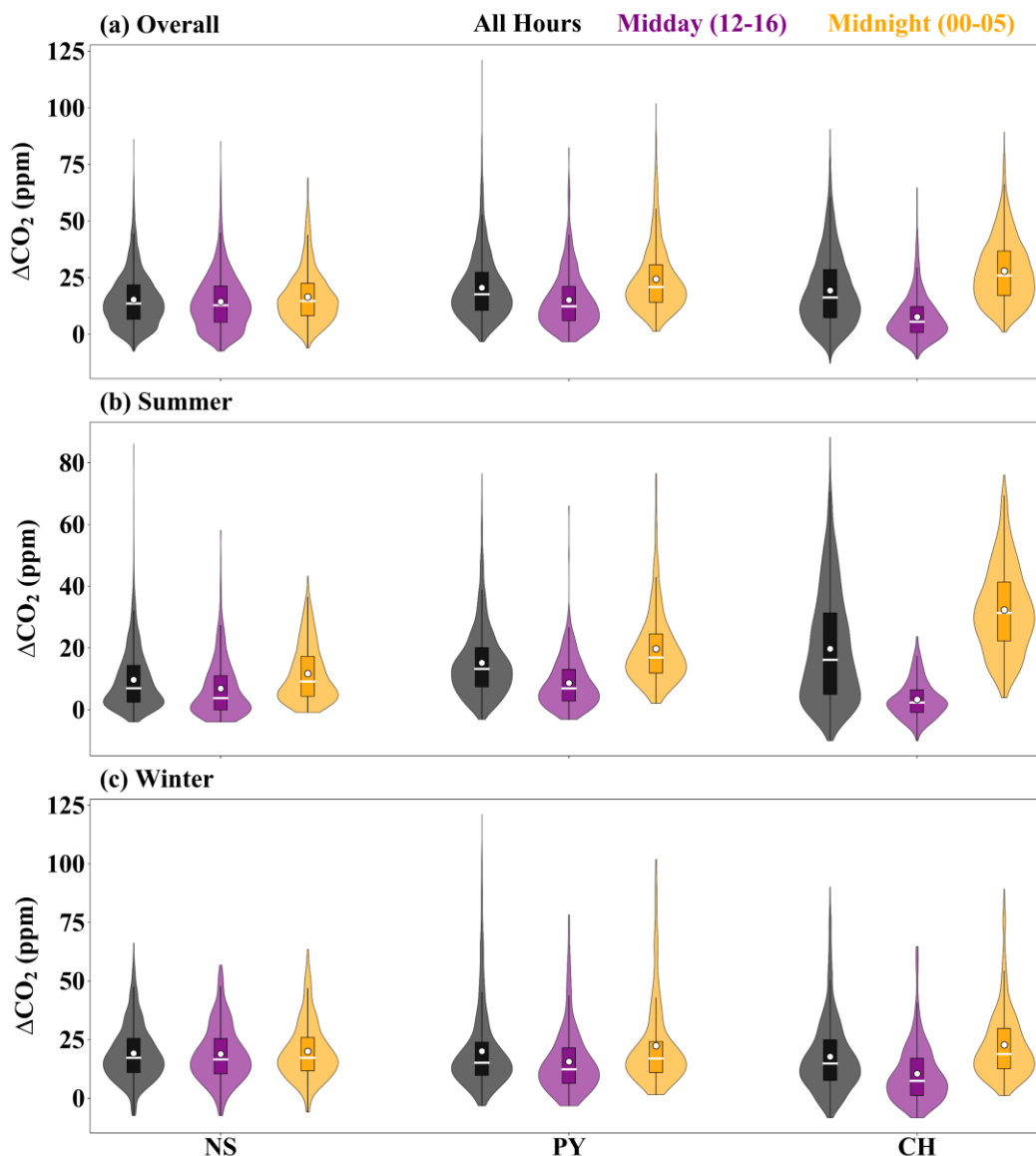
516 CO provides a combustion-specific tracer to further diagnose SLB modulation of anthropogenic signals (Fig. S11
517 in the Supplement). In spring and winter, CO is generally lower on SLBD than on NSLBD, consistent with
518 enhanced dilution and export by the breeze circulation, broadly mirroring the CO₂ behavior (Fig. 7). In autumn, the
519 CO response is weaker and transitional, with only modest daytime reductions. In summer, however, SLB days
520 exhibit a pronounced afternoon CO build-up, with a much larger relative enhancement than CO₂ (relative to the
521 seasonal 24 h mean on NSLBD: ~ 10 % for CO versus ~ 0.7 % for CO₂), implying trapping/recirculation of fresh
522 combustion plumes under weak-wind, shallow-mixing conditions. Overall, the joint CO–CO₂ behavior confirms
523 that SLB exerts a seasonally varying control on near-surface carbon signals—ventilating in cooler seasons but
524 favoring accumulation under the stagnant summer regime.

525 3.3 CO₂ enhancements and uncertainties

526 Figure S12 (in the Supplement) presents the time series of observed CO₂ and CO concentrations at Guangzhou’s
527 stations relative to marine backgrounds from January 1 to December 27, 2023. Compared to urban observations
528 with significant hourly variability, marine background concentrations in Guangzhou remained stable, with summer
529 and winter CO₂ standard deviations of 0.94 ppm and 0.67 ppm, respectively, indicating minimal local source/sink
530 influences. Using Eqs. (13) and (14), marine background uncertainties were calculated (Table S4 in the
531 Supplement). Summer and winter CO₂ marine background uncertainties were 0.96 ppm and 0.70 ppm, respectively,
532 constraining urban marine background uncertainties below 1 ppm—slightly lower than Los Angeles’s 1.4 ppm
533 (Verhulst et al., 2017). CO marine background uncertainties were 12.68 ppb (summer) and 18.36 ppb (winter).

534
535 Based on background concentrations, CO₂ enhancements were derived for all stations. Figure 8 shows
536 enhancements across all hours, afternoon (12:00–16:00), and midnight (00:00–05:00) periods in 2023, summer,
537 and winter. Annual median enhancements were 13.59 (NS), 17.70 (PY), and 16.29 ppm (CH), with pronounced
538 spatiotemporal variability—closely aligning with the 10–20 ppm range observed annually in the Beijing–Tianjin–
539 Hebei (BTH) urban cluster of China (Han et al., 2024). In summer, the all-hours enhancement followed a south-to-
540 north gradient: 7.00 (NS), 13.23 (PY), and 16.91 ppm (CH). This inland maximum likely reflects the combined
541 influence of coastal transport, biogenic exchange, and boundary-layer mixing, and is consistent with the seasonal
542 gradient displacement discussed in Sect. 3.1 (Fig. 3). Afternoon enhancements peaked at PY (6.92 ppm), whereas

543 midnight enhancements at CH reached 31.36 ppm. Winter afternoon enhancements reversed this pattern: 16.58
 544 (NS), 12.37 (PY), and 7.45 ppm (CH), with NS and PY values 4.39 times and 1.79 times higher than summer.
 545 Midnight enhancements at CH remained highest in winter (18.87 ppm), despite a 38.93 % reduction from summer.



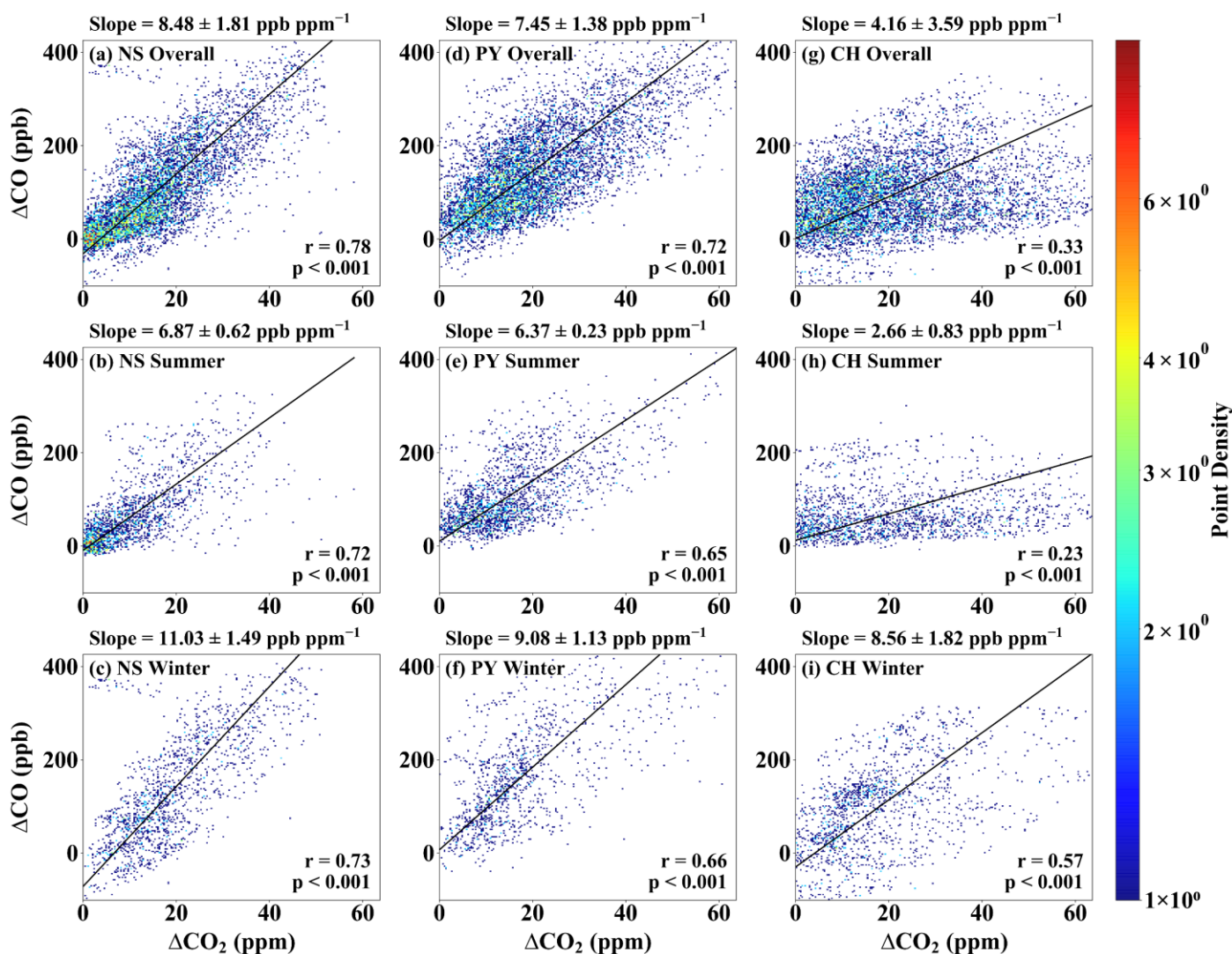
546
 547 **Figure 8.** Distributions of hourly CO₂ enhancement (ΔCO_2) above the background concentrations at NS, PY, and CH
 548 during the (a) overall, (b) summer, and (c) winter periods, shown for all hours, midday (12:00–16:00 LT), and midnight
 549 (00:00–05:00 LT). White dots denote the mean values, and white horizontal lines denote the median values.

550 This spatiotemporal variability reflects divergent influences of anthropogenic emissions, biogenic fluxes, and
 551 atmospheric mixing. At CH, strong diurnal shifts in enhancements (e.g., 31.36 ppm summer midnight) highlight
 552 biogenic dominance, with long-tailed distributions (Fig. 8). Stable, shallow nighttime boundary layers trapped
 553 respiratory emissions near the surface, consistent with isotopic studies in Xi'an (32.80 ppm) and Switzerland (30.00
 554 ppm) (Wang et al., 2021; Berhanu et al., 2017). At NS, transport dominated: summer southerly marine air masses
 555 reduced enhancements, while winter northerly winds transported urban emissions downstream, raising NS

556 enhancements to PY levels (exceeding PY in afternoons). PY's enhancements were primarily anthropogenic,
 557 validated by CO co-variation. CO, a tracer for combustion-derived CO₂, showed significantly higher concentrations
 558 at PY (Fig. S12). PY's median midnight CO enhancements in summer were 2.04 times and 1.43 times higher than
 559 NS and CH (Fig. S13 in the Supplement). Shallow nocturnal boundary layers localized anthropogenic CO near the
 560 surface, with minimal vertical/horizontal transport, confirming PY's anthropogenic dominance.

561 3.4 Continuous observations of $\Delta\text{CO}/\Delta\text{CO}_2$ ratios

562 Reduced Major Axis regression (Model II) was applied to analyze the relationship between CO (ΔCO) and CO₂
 563 (ΔCO_2) concentration enhancements across stations, with the $\Delta\text{CO}/\Delta\text{CO}_2$ emission ratio (R_{CO}) derived from
 564 regression slopes (Fig. 9). In 2023, R_{CO} values for NS, PY, and CH were 8.48 ± 1.81 , 7.45 ± 1.38 , and 4.16 ± 3.59
 565 ppb ppm^{-1} , respectively, with correlation coefficients of 0.78, 0.72, and 0.33, indicating significant spatiotemporal
 566 heterogeneity. Summer R_{CO} was generally lower than winter, with CH exhibiting the lowest seasonal value ($2.66 \pm$
 567 $0.83 \text{ ppb ppm}^{-1}$). Winter maxima occurred at NS ($11.03 \pm 1.49 \text{ ppb ppm}^{-1}$), followed by PY ($9.08 \pm 1.13 \text{ ppb ppm}^{-1}$)
 568 and CH ($8.56 \pm 1.82 \text{ ppb ppm}^{-1}$).



569

570 **Figure 9.** Seasonal relationships between ΔCO_2 and ΔCO enhancements at the (a–c) NS, (d–f) PY, and (g–i) CH stations,
571 analyzed using geometric-mean regression. Panels are shown as two-dimensional (2-D) histogram density plots (hist2d; 200
572 \times 200 bins), where color indicates the number of paired observations per bin. The fitted slope represents the $\Delta\text{CO}/\Delta\text{CO}_2$
573 emission ratio (R_{CO} ; ppb ppm⁻¹), reported as mean \pm 1 SD (reflecting temporal variability).

574 Comparatively, Beijing’s urban R_{CO} in 2019 was measured at 10.46 ± 0.11 ppb ppm⁻¹ using portable Fourier-
575 transform spectroscopy (Che et al., 2022a), while Shanghai and Los Angeles showed 10.22 ± 0.40 and 9.64 ± 0.46
576 ppb ppm⁻¹, respectively, based on satellite and model data (Wu et al., 2022a). Guangzhou’s lower R_{CO} is consistent
577 with the post-2013 tightening of China’s air-quality management across the energy and transport sectors, rather
578 than a single intervention. National action plans (2013–2017 Air Pollution Prevention and Control Action Plan;
579 2018–2020 Three-Year “Blue-Sky” Action Plan) strengthened coal/industrial and vehicle-emission controls with
580 explicit targets and timelines. In parallel, ultra-low-emission (ULE) retrofits of coal-fired power units were rolled
581 out through 2020, and China 6 (VI) on-road emission standards were phased in, with large cities (including
582 Guangzhou) leading implementation; Guangdong’s provincial Blue-Sky measures further reinforced
583 industrial/mobile-source controls and promoted fleet electrification. These measures coincide with independent
584 inventory evidence of declining national CO emissions ($\sim 23\%$ during 2013–2017) (Zheng et al., 2018), plausibly
585 reducing CO/CO₂ emission ratios from dominant urban sources. Consistently, Beijing’s R_{CO} decreased from > 30
586 ppb ppm⁻¹ in 2006 (Han et al., 2009) to 10.22 ± 0.40 ppb ppm⁻¹ by 2020 (Wu et al., 2022a), with additional
587 reductions during the 2008 Olympics and 2020 COVID-19 lockdowns (Wang et al., 2010; Cai et al., 2021). In
588 Guangdong, restrictions on coal plants, retirement of inefficient industries, and promotion of electric vehicles
589 coincided with large declines in SO₂ and NO₂ (85% and 35% in 2019 relative to 2006) (Hu et al., 2021), and Mai
590 et al. (2021) likewise reported improved combustion efficiency in the PRD associated with advances in gasoline
591 vehicles. We emphasize that this interpretation is consistency-based rather than a formal causal identification; fuel
592 mix, fleet composition, and atmospheric oxidation may also contribute (Young et al., 2023; Vimont et al., 2019).

593
594 Seasonal R_{CO} variations stem from biogenic exchange and transport dynamics. Summer’s weaker ΔCO – ΔCO_2
595 correlations at CH reflect dominant biogenic influences (daytime uptake and nighttime respiration), as reported in
596 Beijing, Indianapolis, and Switzerland (Turnbull et al., 2015; Berhanu et al., 2017; Che et al., 2022a). Biogenic
597 impacts decreased from suburban $>$ urban $>$ coastal, aligning with vegetation gradients. Winter’s higher R_{CO} at CH
598 and NS correlated with reduced biogenic activity and northerly transport of urban emissions under stable boundary
599 layers. Berhanu et al. (2017) attributed winter R_{CO} increases to cold-air advection and boundary layer accumulation.
600 NS’s winter R_{CO} (4.16 ppb ppm⁻¹ higher than summer) linked to urban air mass origins, while PY’s seasonal shifts
601 reflected suburban source–sink variations. Although secondary CO from upwind Volatile Organic Compounds

602 (VOCs) and Methane (CH₄) oxidation could perturb R_{CO}, their combined contribution was merely 1 % in coastal
603 urban regions (Griffin et al., 2007).

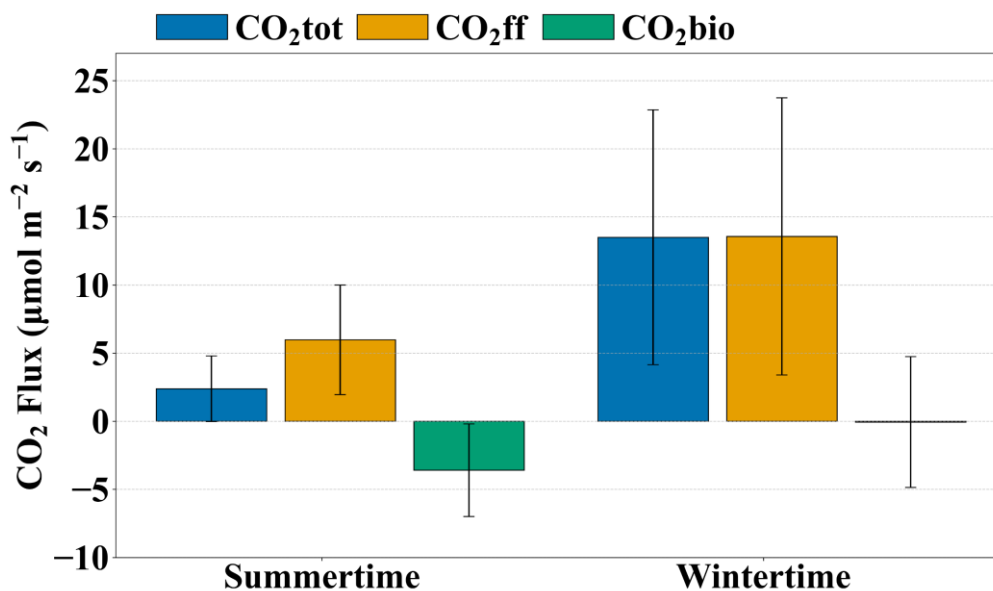
604 **3.5 Partitioning anthropogenic and biogenic fluxes**

605 Section 3.4 shows that the sites differ in how well the $\Delta\text{CO}-\Delta\text{CO}_2$ relationship reflects fossil-fuel combustion. At
606 CH, especially in summer, CO₂ variability is strongly influenced by biogenic exchange, which weakens the
607 combustion linkage implied by R_{CO} and can bias an R_{CO}-based fossil-fuel estimate. At NS, in contrast, variability
608 is dominated by changing transport and upwind air mass origin, particularly in winter when urban plumes frequently
609 reach the coastal site. We therefore select PY—the urban-core site with a comparatively robust combustion signal—
610 to quantify the surface CO₂ emissions (CO₂tot) constrained by the observed concentration enhancements and
611 footprint-informed transport. Using the PY-specific R_{CO}, we then partition CO₂tot into fossil-fuel (CO₂ff) and
612 biogenic (CO₂bio) components.

613

614 Figure 10 summarizes mean afternoon (12:00–16:00 LT) CO₂tot, CO₂ff, and CO₂bio at PY for July 2023 (summer)
615 and December 2023 (winter). Bars show monthly means of daily afternoon values. The plotted error bars indicate
616 ± 1 standard deviation (SD) across days and thus represent day-to-day variability in ventilation, mixing, and
617 transport rather than uncertainty of the monthly mean. Mean uncertainty is quantified by the standard error (SE),
618 which is distinct from the SD shown in Fig. 10. In July, CO₂tot = 2.38 ± 0.45 , CO₂ff = 5.97 ± 0.75 , and CO₂bio =
619 $-3.59 \pm 0.63 \mu\text{mol m}^{-2} \text{s}^{-1}$ (mean \pm SE), whereas in December CO₂tot = 13.50 ± 2.20 , CO₂ff = 13.56 ± 2.40 , and
620 CO₂bio = $-0.06 \pm 1.13 \mu\text{mol m}^{-2} \text{s}^{-1}$ (Table S5). Because CO₂bio is diagnosed as a residual (CO₂bio = CO₂tot –
621 CO₂ff), its uncertainty reflects propagated uncertainties from both CO₂tot and CO₂ff—including measurement and
622 background-selection uncertainty and R_{CO}-related variability—rather than being independent. Notably, December
623 CO₂bio is close to zero. The bootstrap 95 % CI of the monthly mean is $[-2.28, 2.09] \mu\text{mol m}^{-2} \text{s}^{-1}$, which includes
624 zero, indicating that the net biogenic flux was not statistically distinguishable from zero during winter afternoons,
625 likely reflecting a near-neutral balance between photosynthesis and respiration. In contrast, the July mean CO₂bio
626 remains clearly negative relative to its uncertainty, supporting robust summertime net biogenic uptake despite
627 uncertainty propagation inherent to the residual calculation. When assessed using daily afternoon means, the July–
628 December contrasts are statistically significant for CO₂tot, CO₂ff, and CO₂bio (Welch and Mann–Whitney tests;
629 bootstrap 95 % confidence intervals; Table S5). Robust distributional metrics corroborate this significant seasonal
630 increase despite partial day-to-day overlap: the CO₂ff median increases from 4.33 (IQR: 3.58–7.81) in July to 10.70
631 (IQR: 6.74–18.28) $\mu\text{mol m}^{-2} \text{s}^{-1}$ in December. Across both months, CO₂ff is larger in magnitude than CO₂bio,

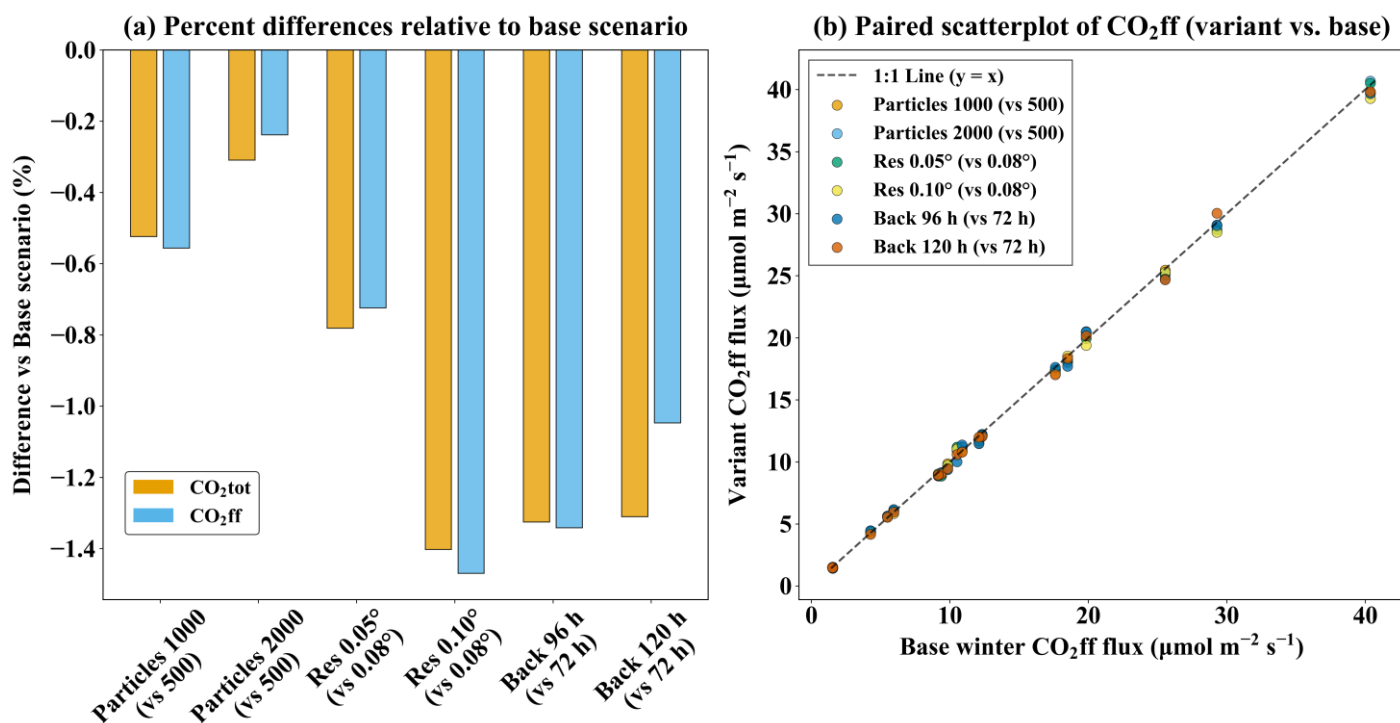
632 implying that the PY afternoon enhancement is primarily fossil-fuel driven, consistent with fossil-dominated urban
 633 enhancements reported for other Chinese cities (Wang et al., 2022). The stronger winter CO₂ff relative to summer
 634 is explained mainly by atmospheric dynamics—reduced dilution under weaker marine ventilation and a shallower
 635 boundary layer—while seasonal emission changes (e.g., winter residential energy use) likely provide a secondary
 636 contribution. In contrast, CO₂bio is more negative in summer, consistent with higher summer NDVI (+11 %) and
 637 warmer conditions approaching optimal canopy temperatures (Table S3).



638
 639 **Figure 10.** Average afternoon (12:00–16:00 LT) CO₂tot, CO₂ff, and CO₂bio at PY for July 2023 (summer; n = 29 valid
 640 days) and December 2023 (winter; n = 18 valid days). December has fewer valid days because objective QC excluded days
 641 with incomplete afternoon coverage (e.g., instrument downtime/maintenance), so the smaller winter sample reflects data
 642 availability rather than subjective selection. Bars show monthly means of daily afternoon values. Error bars indicate ± 1 SD
 643 across daily afternoon means within each month (day-to-day atmospheric variability), not the SE of the monthly mean; SE
 644 and confidence intervals are reported in Table S5.

645 To test the robustness of the winter fossil-fuel dominance inferred at PY—when combustion signals are strongest—
 646 we reran the winter flux-estimation workflow using paired daily afternoon means (12:00–16:00 LT). We then varied
 647 (1) particle number (1000/2000), (2) grid spacing (0.05°/0.10°), and (3) backward duration (96/120 h) relative to
 648 the baseline (500 particles, 0.08°, 72 h). Mean changes were small for both components (Table S6 in the Supplement;
 649 Fig. 11a). Increasing particle number to 1000/2000 changed CO₂ff by -0.56 %/-0.24 % and CO₂tot by
 650 -0.52 %/-0.31 %. Refining the grid to 0.05° yielded comparably small decreases (CO₂ff: -0.72 %; CO₂tot:
 651 -0.78 %). Extending the backward duration to 96/120 h produced changes of -1.34 %/-1.05 % for CO₂ff and
 652 -1.33 %/-1.31 % for CO₂tot. Only the coarser 0.10° grid produced a statistically detectable, yet small, decrease
 653 (CO₂ff: -1.47 %, p = 0.0269; CO₂tot: -1.40 %, p = 0.0164). All other settings yielded changes ≤ 1.34 % with 95 %
 654 CIs spanning zero (p ≥ 0.083), indicating no evidence of material bias at our sample size. Day-to-day consistency

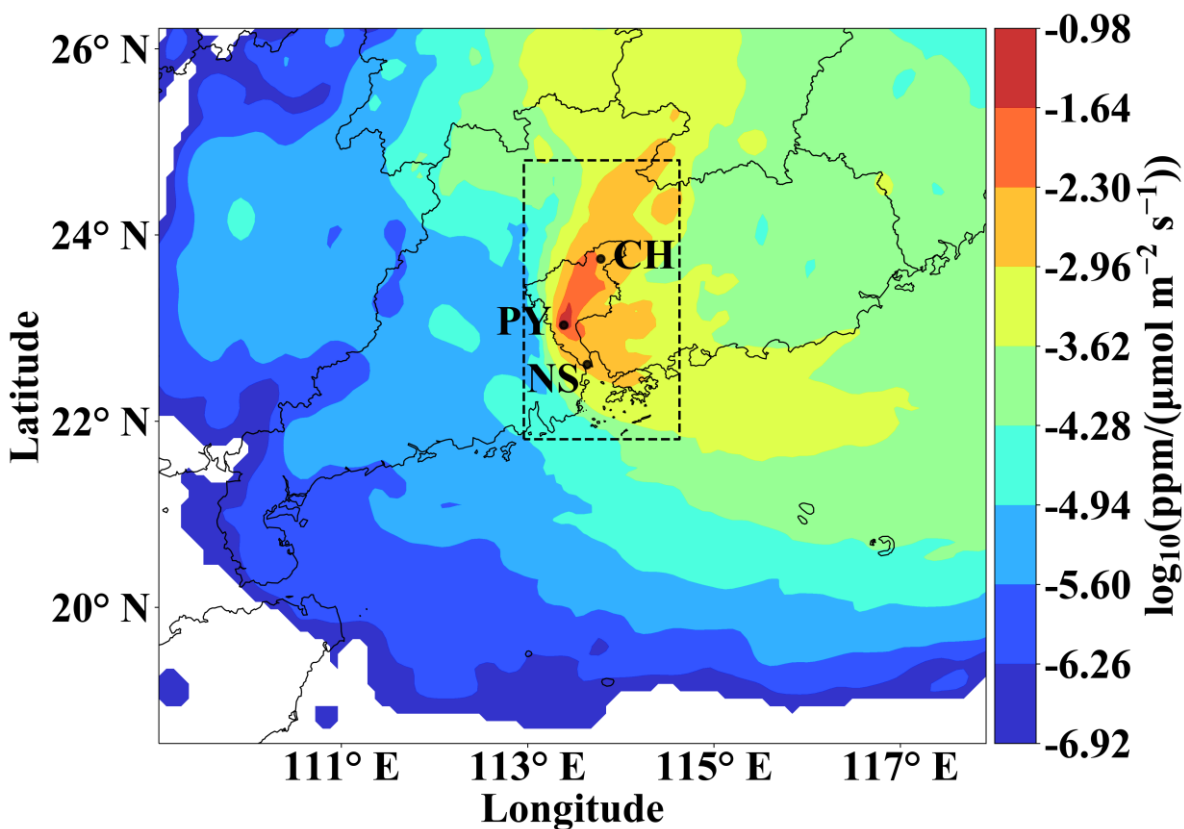
655 remained essentially unchanged across settings, with extremely high correlations (CO_2ff : $r = 0.9993$ – 0.9997 ;
 656 CO_2tot : $r = 0.9992$ – 0.9997) and small RMSE values (CO_2ff : 0.31 – $0.45 \mu\text{mol m}^{-2} \text{s}^{-1}$; CO_2tot : 0.28 – $0.45 \mu\text{mol m}^{-2}$
 657 s^{-1}), consistent with the near-1:1 paired scatter (Fig. 11b). Because wintertime CO_2bio at PY was close to zero,
 658 percent differences were not informative; in absolute terms, test–baseline differences in CO_2bio remained small
 659 (order $10^{-2} \mu\text{mol m}^{-2} \text{s}^{-1}$) with 95 % CIs generally spanning zero, consistent with the tight across-run daily spread
 660 (median $0.045 \mu\text{mol m}^{-2} \text{s}^{-1}$; IQR 0.016 – $0.067 \mu\text{mol m}^{-2} \text{s}^{-1}$) (Table S7 in the Supplement). Across the baseline
 661 plus six variants, the day-by-day ensemble spread was tightly bounded (median 0.20 – $0.21 \mu\text{mol m}^{-2} \text{s}^{-1}$, median
 662 $\text{CV} \approx 1.8 \%$). Together, these results indicate that our baseline STILT configuration lies in a converged regime and
 663 that the inferred winter CO_2ff dominance is robust to reasonable transport-parameter choices.



664
 665 **Figure 11.** STILT parameter sensitivity at PY (winter). **(a)** Mean percent difference (variant – baseline) of inferred fluxes
 666 relative to the winter baseline (500 particles, 0.08° , 72 h), computed from paired daily afternoon means (12:00–16:00 LT; $n =$
 667 18); $\Delta \% = (\text{variant} - \text{base}) / \text{base} \times 100$; negative values indicate lower than baseline. **(b)** Paired scatter of CO_2ff ($\mu\text{mol m}^{-2}$
 668 s^{-1}) from each variant versus the baseline for the same days; solid line is 1:1 ($y = x$).

669 For winter afternoons at PY, measurement and background-selection uncertainties—estimated by propagating their
 670 combined enhancement uncertainty through Eqs. (12)–(14)—contribute only $\sim 0.36 \mu\text{mol m}^{-2} \text{s}^{-1}$, i.e., $\sim 3 \%$ of
 671 the mean winter-afternoon CO_2ff . Paired-day STILT sensitivity tests (Fig. 11) further indicate that the winter-
 672 afternoon CO_2ff attribution is robust to reasonable transport-parameter choices. The remaining uncertainty is thus
 673 more likely dominated by residual transport representation error and coastal mesoscale flow (e.g., wind and
 674 boundary-layer mixing biases), as documented for winter conditions in meteorological/transport modeling (Yadav
 675 et al., 2021; Lin et al., 2021). To provide independent context, we benchmark our winter-afternoon estimate against

676 bottom-up inventories, which are used solely for contextual comparison and do not enter the CO₂ partitioning. We
 677 use 2023 inventories at 0.1° × 0.1° resolution, temporally disaggregate annual totals to hourly emissions using the
 678 same profiles (Crippa et al., 2020), and compute the winter-afternoon (12:00–16:00 LT) mean emission flux over
 679 the winter footprint-defined sensitivity region (Fig. 12). This yields 19.81 μmol m⁻² s⁻¹ from the
 680 EDGAR_2024_GHG (2023) inventory (Crippa et al., 2024) and 85.46 μmol m⁻² s⁻¹ from the MEIC-global-CO₂
 681 (2023) inventory (Xu et al., 2024). While this aligns qualitatively with higher MEIC estimates reported for
 682 Guangdong Province (Yang et al., 2025), the contrast is larger for our winter-afternoon sensitivity region. This
 683 likely reflects differences in spatial disaggregation and point-source representation (e.g., road-network allocation
 684 and power-plant locations) that can be accentuated at sub-provincial scales (Yang et al., 2025).



685
 686 **Figure 12.** Spatial distribution of the mean winter-afternoon (12:00–16:00 LT) STILT footprint at the PY station,
 687 representing the receptor sensitivity to upwind surface fluxes. Colors denote the log₁₀-transformed footprint sensitivity (ppm
 688 / (μmol m⁻² s⁻¹)). The dashed rectangle outlines the sensitivity region used for inventory flux aggregation and benchmarking
 689 in Sect. 3.5.

690 Notably, our observation-based CO₂ff reflects the footprint-weighted enhancement sampled at PY during winter
 691 afternoons after background removal, whereas inventories provide gridded emission fields from which an
 692 unweighted domain-mean afternoon flux can be computed over the sensitivity region. Because only grid cells with
 693 substantial STILT footprint influence contribute materially to the receptor enhancement—and these weights are
 694 highly heterogeneous and transport-dependent (Fig. 12)—the unweighted domain-mean inventory flux may be non-

695 uniformly represented in the receptor signal under variable coastal transport (Gerbig et al., 2003; Lin et al., 2003;
696 Fasoli et al., 2018). Accordingly, an effective footprint-weighted mean flux estimate inferred from the receptor
697 enhancement can differ from the unweighted afternoon-mean inventory flux over the sensitivity region. This
698 difference depends on the spatial alignment between heterogeneous transport footprints and spatially heterogeneous
699 emissions (including localized hotspots), because under a given transport regime many grid cells within the domain
700 may carry negligible footprint influence (Hüser et al., 2017; Kunik et al., 2019). We therefore interpret inventory
701 comparisons as a plausibility envelope that reflects inter-inventory spread, rather than a validation target. Such
702 inventory–observation differences are also reported for other coastal urban basins (e.g., Los Angeles) and are often
703 sensitive to boundary-layer representation and meteorological inputs (Kim et al., 2025).

704

705 Beyond the winter fossil-fuel benchmark above, we further place the summer biogenic component and its offset
706 ratio in the context of independent regional and urban estimates. Summer afternoons exhibited mean CO_2^{bio} of
707 $-3.59 \pm 0.63 \mu\text{mol m}^{-2} \text{s}^{-1}$, consistent with observation-based Pearl River Delta NEE (-0.1 to $-12 \mu\text{mol m}^{-2} \text{s}^{-1}$)
708 (Mai et al., 2024a), and with modeled urban biogenic flux ranges (0 to $-15 \mu\text{mol m}^{-2} \text{s}^{-1}$) reported in previous
709 studies (Wu et al., 2021; Wei et al., 2022; Kim et al., 2025). Consequently, summer-afternoon biogenic uptake
710 offsets 60.13 % of concurrent CO_2^{ff} at PY, with a bootstrap 95 % confidence interval of 48–72 %, highlighting
711 substantial biogenic modulation of coastal urban CO_2 signals. Importantly, the inferred summertime offset remains
712 substantial within the estimated uncertainty range, indicating robust biogenic modulation in magnitude.
713 Comparable growing-season offsets have been reported for other coastal urban regions using independent
714 approaches. A sensor-network combined with box-model analysis for Los Angeles suggests up to 60 % daytime
715 offset; an inversion for the Boston coastal region indicates > 50 % summer-afternoon offset (Kim et al., 2025;
716 Sargent et al., 2018). High-resolution vegetation modeling for New York City similarly suggests ~ 40 % offset of
717 afternoon anthropogenic enhancements and the potential to fully balance on-road traffic contributions (Wei et al.,
718 2022). Overall, these contextual comparisons provide an external plausibility check and indicate that strong
719 growing-season biogenic uptake is a plausible and important modulator of coastal-urban CO_2 signals in Guangzhou.

720 **4 Conclusions**

721 We develop an observation-driven framework to interpret coastal megacity CO_2 dynamics in Guangzhou (January
722 2023–September 2024) using multi-site CO_2/CO measurements, footprint-informed transport analysis, and a site-
723 specific $\Delta\text{CO}/\Delta\text{CO}_2$ (R_{CO}) relationship, without assimilating emission inventories. The three-site gradient reveals
724 contrasting dominant controls by setting: transport governs the largest seasonal amplitude at the coastal site,

725 biogenic exchange drives pronounced summertime daytime drawdown at the vegetated site, and combustion
726 dominates variability in the urban core. This combustion signal is characterized by a regression-derived R_{CO} ,
727 broadly consistent with a regional shift toward cleaner fuels and stricter vehicle-emission controls. Importantly,
728 these patterns point to a seasonally displaced “coastal CO₂ dome”. In contrast to the traditional paradigm in which
729 the maximum CO₂ enhancement is anchored over the urban center, our results show that the dome peak can shift
730 away from the urban core. This shift reflects the combined effects of seasonal coastal transport/mixing and
731 seasonally varying biogenic exchange associated with urban greening, underscoring the dynamic nature of coastal
732 greenhouse gas distributions.

733

734 Under prevailing fair-weather coastal mesoscale conditions, the SLB circulation exerts a key control on diurnal
735 variability in near-surface CO₂ and CO, with a non-linear seasonal modulation. In spring and winter, SLB
736 strengthens ventilation and lowers CO₂, whereas in summer it can favor accumulation under weak-wind, stable
737 conditions. Consistent with this, CO exhibits a more pronounced daytime enhancement than CO₂ during SLB days
738 in summer, supporting a trapping/recirculation regime in which combustion plumes are retained when coastal
739 mesoscale flows coincide with shallow mixing and stable stratification. These seasonally opposing SLB impacts
740 may be overlooked because many urban CO₂ studies focus on inland settings or annual-mean signals. Our results
741 show that coastal mesoscale circulations can reverse the sign of SLB effects across seasons, highlighting important
742 implications for inversion design and interpretation in coastal cities.

743

744 Source–sink attribution at PY indicates that winter-afternoon CO₂ff estimates are robust to measurement
745 uncertainty and background selection, with only minor sensitivity to the tested transport-model configurations. This
746 supports the reliability of our framework for this coastal megacity setting under the adopted sampling and
747 background definition. In summer afternoons, inferred CO₂bio shows substantial biogenic uptake that offsets ~
748 60 % of the concurrent CO₂ff during the peak growing season. This summertime offset aligns with independent
749 estimates for other coastal urban regions, supporting the plausibility of our source–sink separation and suggesting
750 that strong biogenic modulation can persist even under complex SLB-driven coastal transport.

751

752 Several limitations remain. The three-site network cannot resolve hyperlocal source heterogeneity, and SLB
753 identification relies on near-surface wind criteria rather than the full 3-D boundary-layer structure. Although
754 configuration sensitivity is small, transport uncertainties associated with winds and boundary-layer mixing are not
755 fully quantified here. In addition, CO-based attribution is sensitive to variability in R_{CO} arising from changing

756 source mix, plume processing, and background definition, which propagates into inferred CO₂ff and the residual
757 CO₂bio. Future work combining denser low-cost networks, boundary-layer profiling, and periodic isotopic
758 constraints would further tighten coastal urban carbon budgets.

759

760 Overall, coastal mesoscale dynamics can invert the seasonal role of SLB—from ventilation in cool seasons to
761 trapping/recirculation in summer—thereby reshaping urban CO₂ signals in coastal megacities. Meanwhile, a
762 substantial summertime biogenic offset associated with urban greening can strongly damp apparent fossil-fuel
763 signals and should be considered when evaluating mitigation trends. These findings have direct implications for
764 coastal urban monitoring and policy evaluation: to avoid season-dependent biases in assessing mitigation progress,
765 urban monitoring networks should prioritize the decoupling of biogenic signals—particularly during summer—to
766 accurately isolate anthropogenic contributions and thus ensure reliable evaluation of mitigation progress.
767 Furthermore, the strategic selection of monitoring sites in coastal megacities must explicitly account for the non-
768 linear accumulation effects of SLB circulations to ensure long-term sampling representativeness. While our
769 framework does not produce posterior flux fields as in a formal Bayesian inversion, it provides a complementary,
770 observation-driven tool for rapid process attribution and consistency checking in coastal urban carbon monitoring
771 and mitigation assessment.

772 **Code and data availability.** The STILT model source code used in this paper has been published on Zenodo and
773 can be accessed at <https://doi.org/10.5281/zenodo.1196561> (Fasoli, 2018). The EDGAR data used in this study are
774 publicly available at https://edgar.jrc.ec.europa.eu/dataset_ghg2024#conditions
775 (last access: 18 June 2025)(Crippa et al., 2024). The planetary boundary layer height data used in this study are available at
776 <https://doi.org/10.24381/cds.adbb2d47> (Hersbach, 2023). The NDVI data used in this study are available at
777 <https://doi.org/10.5067/MODIS/MOD13A3.006> (Didan, 2015). The CarbonTracker (CT-NRT.v2024-5) products
778 are available online at <https://doi.org/10.15138/ATPD-K925> (Jacobson et al., 2024). The NOAA Earth System
779 Research Laboratory/Global Monitoring Laboratory (NOAA GML) data used in this study are available at
780 <https://doi.org/10.25925/20241101> (Schuldt et al., 2024). Additional data and information used in this study are
781 available from the corresponding author upon request.

782 **Author contributions.** JWZ and ML designed the study. JWZ, YJL, CLP, BH, YYH, XFL, SJS, CLC, CW, ZZ,
783 JJL and ML contributed to data collection and data analysis. JWZ designed and performed the model simulations.
784 JWZ and ML wrote the paper with contributions from all coauthors. JJL and SJS provided valuable feedback and
785 opinions for paper refinement. All the authors revised the paper and edited the text.

786 **Competing interests.** The contact author has declared that none of the authors has any competing interests.

787 **Disclaimer.** Publisher's note: Copernicus Publications remains neutral with regard to jurisdictional claims in

788 published maps and institutional affiliations.

789 **Acknowledgements.** The authors would like to thank the personnel who participated in data collection, instrument
790 maintenance, and logistic support during the field campaign. We also acknowledge the NOAA GML for providing
791 the CO₂ GLOBALVIEWplus v10.1 ObsPack and CarbonTracker CT-NRT.v2024-5 datasets, which were used for
792 monitoring comparison in this study. CarbonTracker CT-NRT.v2024-5 results provided by NOAA GML, Boulder,
793 Colorado, USA from the website at <http://carbontracker.noaa.gov>.

794 **Financial support.** This work was financially supported by the National Natural Science Foundation of China
795 (Grant no. 42477273) and the National Key R&D Program of China (Grant no. 2022YFE0209500).

796 References

- 797 Ahmadov, R., Gerbig, C., Kretschmer, R., Koerner, S., Neining, B., Dolman, A., and Sarrat, C.: Mesoscale covariance of
798 transport and CO₂ fluxes: Evidence from observations and simulations using the WRF - VPRM coupled atmosphere -
799 biosphere model, *J. Geophys. Res.-Atmos.*, 112, <https://doi.org/10.1029/2007JD008552>, 2007.
- 800 Allouche, M., Bou - Zeid, E., and Iipponen, J.: The influence of synoptic wind on land - sea breezes, *Quarterly Journal of the*
801 *Royal Meteorological Society*, 149, 3198-3219, <https://doi.org/10.1002/qj.4552>, 2023.
- 802 Atkins, N. T. and Wakimoto, R. M.: Influence of the synoptic-scale flow on sea breezes observed during CaPE, *Monthly*
803 *weather review*, 125, 2112-2130, [https://doi.org/10.1175/1520-0493\(1997\)125<2112:IOTSSF>2.0.CO;2](https://doi.org/10.1175/1520-0493(1997)125<2112:IOTSSF>2.0.CO;2), 1997.
- 804 Berhanu, T. A., Szidat, S., Brunner, D., Satar, E., Schanda, R., Nyfeler, P., Battaglia, M., Steinbacher, M., Hammer, S., and
805 Leuenberger, M.: Estimation of the fossil fuel component in atmospheric CO₂ based on radiocarbon measurements at the
806 Beromünster tall tower, Switzerland, *Atmos. Chem. Phys.*, 17, 10753-10766, <https://doi.org/10.5194/acp-17-10753-2017>,
807 2017.
- 808 Boon, A., Broquet, G., Clifford, D. J., Chevallier, F., Butterfield, D. M., Pison, I., Ramonet, M., Paris, J.-D., and Ciais, P.:
809 Analysis of the potential of near-ground measurements of CO₂ and CH₄ in London, UK, for the monitoring of city-scale
810 emissions using an atmospheric transport model, *Atmos. Chem. Phys.*, 16, 6735-6756, [https://doi.org/10.5194/acp-16-6735-](https://doi.org/10.5194/acp-16-6735-2016)
811 [2016](https://doi.org/10.5194/acp-16-6735-2016), 2016.
- 812 Briber, B. M., Hutyra, L. R., Dunn, A. L., Raciti, S. M., and Munger, J. W.: Variations in atmospheric CO₂ mixing ratios across
813 a Boston, MA urban to rural gradient, *Land*, 2, 304-327, <https://doi.org/10.3390/land2030304>, 2013.
- 814 Cai, Z., Che, K., Liu, Y., Yang, D., Liu, C., and Yue, X.: Decreased anthropogenic CO₂ emissions during the COVID-19
815 pandemic estimated from FTS and MAX-DOAS measurements at urban Beijing, *Remote Sens.-basel.*, 13, 517,
816 <https://doi.org/10.3390/rs13030517>, 2021.
- 817 Che, K., Liu, Y., Cai, Z., Yang, D., Wang, H., Ji, D., Yang, Y., and Wang, P.: Characterization of regional combustion efficiency
818 using ΔXCO: ΔXCO₂ observed by a portable Fourier-Transform Spectrometer at an urban site in Beijing, *Adv. Atmos. Sci.*,
819 39, 1299-1315, <https://doi.org/10.1007/s00376-022-1247-7>, 2022a.
- 820 Che, K., Cai, Z., Liu, Y., Wu, L., Yang, D., Chen, Y., Meng, X., Zhou, M., Wang, J., Yao, L., and Wang, P.: Lagrangian inversion
821 of anthropogenic CO₂ emissions from Beijing using differential column measurements, *Environ. Res. Lett.*, 17,
822 <https://doi.org/10.1088/1748-9326/ac7477>, 2022b.
- 823 Chen, Y., Ma, Q., Lin, W., Xu, X., Yao, J., and Gao, W.: Measurement report: Long-term variations in carbon monoxide at a
824 background station in China's Yangtze River Delta region, *Atmos. Chem. Phys.*, 20, 15969-15982,
825 <https://doi.org/10.5194/acp-20-15969-2020>, 2020.
- 826 Chen, Y., Lu, Y., Qi, B., Ma, Q., Zang, K., Lin, Y., Liu, S., Pan, F., Li, S., and Guo, P.: Atmospheric CO₂ in the megacity
827 Hangzhou, China: Urban-suburban differences, sources and impact factors, *Sci. Total Environ.*, 926, 171635,
828 <https://doi.org/10.1016/j.scitotenv.2024.171635>, 2024.

829 Corro, L. M., Bagstad, K. J., Heris, M. P., Ibsen, P. C., Schleeweis, K. G., Diffendorfer, J. E., Troy, A., Megown, K., and
830 O'Neil-Dunne, J. P. M.: An enhanced national-scale urban tree canopy cover dataset for the United States, *Sci Data*, 12, 490,
831 <https://doi.org/10.1038/s41597-025-04816-0>, 2025.

832 Crippa, M., Solazzo, E., Huang, G., Guizzardi, D., Koffi, E., Muntean, M., Schieberle, C., Friedrich, R., and Janssens-
833 Maenhout, G.: High resolution temporal profiles in the Emissions Database for Global Atmospheric Research, *Scientific*
834 *Data*, 7, <https://doi.org/10.1038/s41597-020-0462-2>, 2020.

835 Crippa, M., Guizzardi, D., Pisoni, E., Solazzo, E., Guion, A., Muntean, M., Florczyk, A., Schiavina, M., Melchiorri, M., and
836 Hutfilter, A. F.: Global anthropogenic emissions in urban areas: patterns, trends, and challenges, *Environ. Res. Lett.*, 16,
837 <https://doi.org/10.1088/1748-9326/ac00e2>, 2021.

838 Crippa, M., Guizzardi, D., Pagani, F., Banja, M., Muntean, M., Schaaf, E., Monforti-Ferrario, F., Becker, W. E., Quadrelli, R.,
839 Riquez Martin, A., Taghavi-Moharamli, P., Köykkä, J., Grassi, G., Rossi, S., Melo, J., Oom, D., Branco, A., San-Miguel,
840 J., Manca, G., Pisoni, E., Vignati, E., and Pekar, F.: GHG emissions of all world countries, Publications Office of the
841 European Union, <https://doi.org/10.2760/4002897>, 2024.

842 Deng, A., Lauvaux, T., Davis, K. J., Gaudet, B. J., Miles, N., Richardson, S. J., Wu, K., Sarmiento, D. P., Hardesty, R. M., and
843 Bonin, T. A.: Toward reduced transport errors in a high resolution urban CO₂ inversion system, *Elem Sci Anth*, 5, 20,
844 <https://doi.org/10.1525/elementa.133>, 2017.

845 Didan, K.: MOD13A3 MODIS/Terra Vegetation Indices Monthly L3 Global 1km SIN Grid V006, NASA Land Processes
846 Distributed Active Archive Center [dataset], <https://doi.org/10.5067/MODIS/MOD13A3.006>, 2015.

847 Dusenge, M. E., Duarte, A. G., and Way, D. A.: Plant carbon metabolism and climate change: elevated CO₂ and temperature
848 impacts on photosynthesis, photorespiration and respiration, *New Phytol.*, 221, 32-49, <https://doi.org/10.1111/nph.15283>,
849 2019.

850 Fasoli, B.: uataq/stilt: Geoscientific Model Development 2018 (v1.0), Zenodo [code], <https://doi.org/10.5281/zenodo.1196561>,
851 2018.

852 Fasoli, B., Lin, J. C., Bowling, D. R., Mitchell, L., and Mendoza, D.: Simulating atmospheric tracer concentrations for spatially
853 distributed receptors: updates to the Stochastic Time-Inverted Lagrangian Transport model's R interface (STILT-R version
854 2), *Geosci. Model Dev.*, 11, 2813-2824, <https://doi.org/10.5194/gmd-11-2813-2018>, 2018.

855 Gao, S., Zhang, X., and Chen, M.: Spatiotemporal dynamics and driving forces of city-level CO₂ emissions in China from
856 2000 to 2019, *J. Clean. Prod.*, 377, 134358, <https://doi.org/10.1016/j.jclepro.2022.134358>, 2022.

857 Gao, Y., Lee, X., Liu, S., Hu, N., Wei, X., Hu, C., Liu, C., Zhang, Z., and Yang, Y.: Spatiotemporal variability of the near-
858 surface CO₂ concentration across an industrial-urban-rural transect, Nanjing, China, *Sci. Total Environ.*, 631, 1192-1200,
859 <https://doi.org/10.1016/j.scitotenv.2018.03.126>, 2018.

860 Gately, C. K. and Hutyra, L. R.: Large Uncertainties in Urban - Scale Carbon Emissions, *J. Geophys. Res.-Atmos.*, 122,
861 <https://doi.org/10.1002/2017jd027359>, 2017.

862 George, K., Ziska, L. H., Bunce, J. A., and Quebedeaux, B.: Elevated atmospheric CO₂ concentration and temperature across
863 an urban-rural transect, *Atmos. Environ.*, 41, 7654-7665, <https://doi.org/10.1016/j.atmosenv.2007.08.018>, 2007.

864 Gerbig, C., Lin, J., Wofsy, S., Daube, B., Andrews, A., Stephens, B., Bakwin, P., and Grainger, C.: Toward constraining
865 regional - scale fluxes of CO₂ with atmospheric observations over a continent: 2. Analysis of COBRA data using a
866 receptor - oriented framework, *J. Geophys. Res.-Atmos.*, 108, <https://doi.org/10.1029/2002JD003018>, 2003.

867 Glauch, T., Marshall, J., Gerbig, C., Botía, S., Galkowski, M., Vardag, S. N., and Butz, A.: pyVPRM: A next-generation
868 Vegetation Photosynthesis and Respiration Model for the post-MODIS era, *Geosci. Model Dev.*, 18, 4713-4742,
869 <https://doi.org/10.5194/gmd-18-4713-2025>, 2025.

870 Griffin, R. J., Chen, J., Carmody, K., Vutukuru, S., and Dabdub, D.: Contribution of gas phase oxidation of volatile organic
871 compounds to atmospheric carbon monoxide levels in two areas of the United States, *J. Geophys. Res.-Atmos.*, 112,
872 <https://doi.org/10.1029/2006JD007602>, 2007.

873 Guangzhou Municipal Bureau of Statistics: Guangzhou Statistical Yearbook 2024, Tech. rep.,
874 https://tjj.gz.gov.cn/datav/admin/home/www_nj/ (last access: 1 December 2025), 2024.

875 Gurney, K. R., Patarasuk, R., Liang, J., Song, Y., O'Keeffe, D., Rao, P., Whetstone, J. R., Duren, R. M., Eldering, A., and Miller,
876 C.: The Hestia fossil fuel CO₂ emissions data product for the Los Angeles megacity (Hestia-LA), *Earth Syst. Sci. Data*, 11,
877 1309-1335, <https://doi.org/10.5194/essd-11-1309-2019>, 2019.

878 Han, P., Yao, B., Cai, Q., Chen, H., Sun, W., Liang, M., Zhang, X., Zhao, M., Martin, C., Liu, Z., Ye, H., Wang, P., Li, Y., and
879 Zeng, N.: Support Carbon Neutral Goal with a High-Resolution Carbon Monitoring System in Beijing, *B. Am. Meteorol.*
880 *Soc.*, 105, E2461-E2481, <https://doi.org/10.1175/bams-d-23-0025.1>, 2024.

881 Han, S., Kondo, Y., Oshima, N., Takegawa, N., Miyazaki, Y., Hu, M., Lin, P., Deng, Z., Zhao, Y., and Sugimoto, N.: Temporal
882 variations of elemental carbon in Beijing, *J. Geophys. Res.-Atmos.*, 114, <https://doi.org/10.1029/2009JD012027>, 2009.

883 Hao, T., Chen, S., Liu, J., Tang, Y., and Han, S.: An observational study on the impact of sea-land breeze and low-level jet on
884 air pollutant transport in the Bohai Bay, *Atmos. Pollut. Res.*, 15, 102143, <https://doi.org/10.1016/j.apr.2024.102143>, 2024.

885 Hao, T., Chen, S., Cai, Z., Shan, X., Meng, L., Han, S., and Dong, G.: Influence of sea breeze on atmospheric pollutant
886 concentration over Tianjin, *China Environmental Science*, 37(9), 3247-3257, <https://doi.org/10.3969/j.issn.1000-6923.2017.09.006>, 2017.

887

888 He, H., Kramer, R. J., Soden, B. J., and Jeevanjee, N.: State dependence of CO₂ forcing and its implications for climate
889 sensitivity, *Science*, 382, 7, <https://doi.org/10.1126/science.abq6872>, 2023.

890 Hersbach, H., Bell, B., Berrisford, P., Biavati, G., Horányi, A., Muñoz Sabater, J., Nicolas, J., Peubey, C., Radu, R., Rozum,
891 I., Schepers, D., Simmons, A., Soci, C., Dee, D., Thépaut, J.-N.: ERA5 hourly data on single levels from 1940 to present,
892 Copernicus Climate Change Service (C3S) Climate Data Store (CDS) [dataset], <https://doi.org/10.24381/cds.adbb2d47>,
893 2023.

894 Hu, M., Wang, Y., Wang, S., Jiao, M., Huang, G., and Xia, B.: Spatial-temporal heterogeneity of air pollution and its
895 relationship with meteorological factors in the Pearl River Delta, China, *Atmos. Environ.*, 254, 118415,
896 <https://doi.org/10.1016/j.atmosenv.2021.118415>, 2021.

897 Huang, Y., Li, S., Zhu, Y., Liu, Y., Hong, Y., Chen, X., Deng, W., Xi, X., Lu, X., and Fan, Q.: Increasing sea - land breeze
898 frequencies over coastal areas of China in the past five decades, *Geophys. Res. Lett.*, 52, e2024GL112480,
899 <https://doi.org/10.1029/2024GL112480>, 2025.

900 Hüser, I., Harder, H., Heil, A., and Kaiser, J. W.: Assumptions about footprint layer heights influence the quantification of
901 emission sources: a case study for Cyprus, *Atmos. Chem. Phys.*, 17, 10955-10967, [https://doi.org/10.5194/acp-17-10955-](https://doi.org/10.5194/acp-17-10955-2017)
902 [2017](https://doi.org/10.5194/acp-17-10955-2017), 2017.

903 Jacobson, A. R., Schuldt, K. N., Andrews, A., Miller, J. B., Oda, T., Basu, S., Mund, J., Weir, B., Ott, L., Aalto, T., Abshire, J.
904 B., Aikin, K., Allen, G., Andrade, M., Apadula, F., Arnold, S., Baier, B., Bakwin, P., Bartyzel, J., Bentz, G., Bergamaschi,
905 P., Beyersdorf, A., Biermann, T., Biraud, S. C., Blanc, P.-E., Boenisch, H., Bowling, D., Brailsford, G., Brand, W. A.,
906 Brunner, D., Bui, T. P., Burban, B., Băni, L., Calzolari, F., Chang, C. S., Chen, H., Chen, G., Chmura, L., Clark, S., Climadat,
907 S., Colomb, A., Commane, R., Condori, L., Conen, F., Conil, S., Couret, C., Cristofanelli, P., Cuevas, E., Curcoll, R., Daube,
908 B., Davis, K. J., De Mazière, M., De Wekker, S., Dean-Day, J. M., Della Coletta, J., Delmotte, M., Di Iorio, T., DiGangi,
909 E., DiGangi, J. P., Dickerson, R., Elsasser, M., Emmenegger, L., Fang, S., Forster, G., France, J., Frumau, A., Fuente-Lastra,
910 M., Galkowski, M., Gatti, L. V., Gehrlein, T., Gerbig, C., Gheusi, F., Gloor, E., Goto, D., Griffis, T., Hammer, S., Hanisco,
911 T. F., Hanson, C., Haszpra, L., Hatakka, J., Heimann, M., Heliasz, M., Heltai, D., Henne, S., Hensen, A., Hermans, C.,
912 Hermansen, O., Hintsa, E., Hoheisel, A., Holst, J., Iraci, L. T., Ivakhov, V., Jaffe, D. A., Jordan, A., Joubert, W., Kang, H.-
913 Y., Karion, A., Kawa, S. R., Kazan, V., Keeling, R. F., Keronen, P., Kim, J., Klausen, J., Kneuer, T., Ko, M.-Y., Kolari, P.,
914 Kominkova, K., Kort, E., Kozlova, E., Krummel, P. B., Kubistin, D., Kulawik, S. S., Kumps, N., Labuschagne, C., Lam, D.
915 H., Lan, X., Langenfelds, R. L., Lanza, A., Laurent, O., Laurila, T., Lauvaux, T., Lavric, J., Law, B. E., Lee, C.-H., Lee, J.,
916 Lehner, I., Lehtinen, K., Leppert, R., Leskinen, A., Leuenberger, M., Leung, W. H., Levin, I., Levula, J., Lin, J., Lindauer,
917 M., Lindroth, A., Loh, Z. M., Lopez, M., Lunder, C. R., Löfvenius, M. O., Machida, T., Mammarella, I., Manca, G., Manning,
918 A., Manning, A., Marek, M. V., Marklund, P., Marrero, J. E., Martin, M. Y., Martin, D., Martins, G. A., Matsueda, H.,
919 McKain, K., Meijer, H., Meinhardt, F., Merchant, L., Metzger, J.-M., Mihalopoulos, N., Miles, N. L., Miller, C. E., Mitchell,
920 L., Monteiro, V., Montzka, S., Moossen, H., Moreno, C., Morgan, E., Morgui, J.-A., Morimoto, S., Munger, J. W., Munro,

921 D., Mutuku, M., Myhre, C. L., Mölder, M., Müller-Williams, J., Nakaoka, S.-I., Necki, J., Newman, S., Nichol, S., Nisbet,
922 E., Niwa, Y., Njiru, D. M., Noe, S. M., Nojiri, Y., O'Doherty, S., Obersteiner, F., Paplawsky, B., Parworth, C. L., Peischl, J.,
923 Peltola, O., Peters, W., Philippon, C., Piacentino, S., Pichon, J. M., Pickers, P., Piper, S., Pitt, J., Plass-Dülmer, C., Platt, S.
924 M., Prinzivalli, S., Ramonet, M., Ramos, R., Ren, X., Reyes-Sanchez, E., Richardson, S. J., Rigouleau, L.-J., Riris, H.,
925 Rivas, P. P., Rothe, M., Roulet, Y.-A., Ryerson, T., Ryoo, J.-M., Sargent, M., Sasakawa, M., Schaefer, H., Scheeren, B.,
926 Schmidt, M., Schuck, T., Schumacher, M., Seibel, J., Seifert, T., Sha, M. K., Shepson, P., Shin, D., Shook, M., Sloop, C. D.,
927 Smale, D., Smith, P. D., Spain, G., St. Clair, J. M., Steger, D., Steinbacher, M., Stephens, B., Sweeney, C., Sørensen, L. L.,
928 Taipale, R., Takatsuji, S., Tans, P., Thoning, K., Timas, H., Torn, M., Trisolino, P., Turnbull, J., Vermeulen, A., Viner, B.,
929 Vitkova, G., Walker, S., Watson, A., Weiss, R., Weyrauch, D., Wofsy, S. C., Worsley, J., Worthy, D., Xueref-Remy, I., Yates,
930 E. L., Young, D., Yver-Kwok, C., Zaehle, S., Zahn, A., Zellweger, C., Zimnoch, M., de Souza, R. A., di Sarra, A. G., van
931 Dinter, D., and van den Bulk, P.: CarbonTracker CT-NRT.v2024-5, NOAA Earth System Research Laboratory [dataset],
932 <https://doi.org/10.15138/atpd-k925>, 2024.

933 Kim, J., Berelson, W. M., Rollins, N. E., Asimow, N. G., Newman, C., Cohen, R. C., Miller, J. B., McDonald, B. C., Peischl,
934 J., and Lehman, S. J.: Observing Anthropogenic and Biogenic CO₂ Emissions in Los Angeles Using a Dense Sensor
935 Network, *Environ Sci Technol*, 59, 3508-3517, <https://doi.org/10.1021/acs.est.4c11392>, 2025.

936 Kumar, P.: Climate change and cities: challenges ahead, *Front. Sustain. Cities*, 3, 645613,
937 <https://doi.org/10.3389/frsc.2021.645613>, 2021.

938 Kunik, L., Mallia, D. V., Gurney, K. R., Mendoza, D. L., Oda, T., and Lin, J. C.: Bayesian inverse estimation of urban CO₂
939 emissions: Results from a synthetic data simulation over Salt Lake City, UT, *Elem Sci Anth*, 7, 36,
940 <https://doi.org/10.1525/elementa.375>, 2019.

941 Lauvaux, T., Miles, N. L., Deng, A., Richardson, S. J., Cambaliza, M. O., Davis, K. J., Gaudet, B., Gurney, K. R., Huang, J.,
942 O'Keefe, D., Song, Y., Karion, A., Oda, T., Patarasuk, R., Razlivanov, I., Sarmiento, D., Shepson, P., Sweeney, C., Turnbull,
943 J., and Wu, K.: High-resolution atmospheric inversion of urban CO₂ emissions during the dormant season of the Indianapolis
944 Flux Experiment (INFLUX), *J. Geophys. Res.-Atmos.*, 121, 5213-5236, <https://doi.org/10.1002/2015JD024473>, 2016.

945 Lei, B.-Q., Li, L., and Chan, P. W.: Long-term trend in the sea-land breeze in Hong Kong, *Urban. Clim.*, 55, 101981,
946 <https://doi.org/10.1016/j.uclim.2024.101981>, 2024.

947 Leroyer, S., Bélair, S., Husain, S. Z., and Mailhot, J.: Subkilometer numerical weather prediction in an urban coastal area: A
948 case study over the Vancouver metropolitan area, *J. Appl. Meteorol. Clim.*, 53, 1433-1453, [https://doi.org/10.1175/JAMC-](https://doi.org/10.1175/JAMC-D-13-0202.1)
949 [D-13-0202.1](https://doi.org/10.1175/JAMC-D-13-0202.1), 2014.

950 Lian, J., Lauvaux, T., Utard, H., Bréon, F.-M., Broquet, G., Ramonet, M., Laurent, O., Albarus, I., Chariot, M., and Kotthaus,
951 S.: Can we use atmospheric CO₂ measurements to verify emission trends reported by cities? Lessons from a 6-year
952 atmospheric inversion over Paris, *Atmos. Chem. Phys.*, 23, 8823-8835, <https://doi.org/10.5194/acp-23-8823-2023>, 2023.

953 Lin, J. C., Bares, R., Fasoli, B., Garcia, M., Crosman, E., and Lyman, S.: Declining methane emissions and steady, high leakage
954 rates observed over multiple years in a western US oil/gas production basin, *Sci. Rep-uk.*, 11, 22291,
955 <https://doi.org/10.1038/s41598-021-01721-5>, 2021.

956 Lin, J. C., Gerbig, C., Wofsy, S., Andrews, A., Daube, B., Davis, K., and Grainger, C.: A near - field tool for simulating the
957 upstream influence of atmospheric observations: The Stochastic Time - Inverted Lagrangian Transport (STILT) model, *J.*
958 *Geophys. Res.-Atmos.*, 108(D16), <https://doi.org/10.1029/2002JD003161>, 2003.

959 Liu, C., Huang, J.-P., Diao, Y.-W., Wen, X.-F., Xiao, W., Zhang, M., Lee, X.-H., and Liu, S.-D.: Optimization and evaluation
960 of vegetation photosynthesis and respiration model using the measurements collected from the forest site of subtropical
961 coniferous-evergreen, *Chinese Journal of Plant Ecology*, 39, 388-397, <https://doi.org/10.17521/cjpe.2015.0038>, 2015.

962 Liu, H., Chan, J. C., and Cheng, A. Y.: Internal boundary layer structure under sea-breeze conditions in Hong Kong, *Atmos.*
963 *Environ.*, 35, 683-692, [https://doi.org/10.1016/S1352-2310\(00\)00335-6](https://doi.org/10.1016/S1352-2310(00)00335-6), 2001.

964 Liu, W., Niu, Z., Feng, X., Zhou, W., Liang, D., Wang, G., and Liu, L.: Determining the key meteorological factors affecting
965 atmospheric CO₂ and CH₄ using machine learning algorithms at a suburban site in China, *Urban. Clim.*, 59, 102312,
966 <https://doi.org/10.1016/j.uclim.2025.102312>, 2025.

967 Ma, M., Gao, Y., Ding, A., Su, H., Liao, H., Wang, S., Wang, X., Zhao, B., Zhang, S., Fu, P., Guenther, A. B., Wang, M., Li,
968 S., Chu, B., Yao, X., and Gao, H.: Development and Assessment of a High-Resolution Biogenic Emission Inventory from
969 Urban Green Spaces in China, *Environ Sci Technol*, 56, 175-184, <https://doi.org/10.1021/acs.est.1c06170>, 2022.

970 Mai, B., Deng, X., Liu, X., Li, T., Guo, J., and Ma, Q.: The climatology of ambient CO₂ concentrations from long-term
971 observation in the Pearl River Delta region of China: Roles of anthropogenic and biogenic processes, *Atmos. Environ.*, 251,
972 118266, <https://doi.org/10.1016/j.atmosenv.2021.118266>, 2021.

973 Mai, B., Diao, Y., Yang, H., Deng, T., Zou, Y., Wang, Y., Lan, W., Liu, X., and Deng, X.: Assessing atmospheric CO₂
974 concentrations and contributions from biogenic and anthropogenic sources in the Pearl River Delta region, *Urban. Clim.*,
975 54, 101864, <https://doi.org/10.1016/j.uclim.2024.101864>, 2024a.

976 Mai, J., Yu, L., Deng, T., Wu, D., Qing, P., and Yu, X.: Impact of sea-land breezes on the ozone pollution over the Pearl River
977 Estuary, *China Environmental Science*, 45(03), 1198-1209, <https://doi.org/10.19674/j.cnki.issn1000-6923.20241102.001>,
978 2024b.

979 Menzer, O. and McFadden, J. P.: Statistical partitioning of a three-year time series of direct urban net CO₂ flux measurements
980 into biogenic and anthropogenic components, *Atmos. Environ.*, 170, 319-333,
981 <https://doi.org/10.1016/j.atmosenv.2017.09.049>, 2017.

982 Miller, J. B., Lehman, S. J., Verhulst, K. R., Miller, C. E., Duren, R. M., Yadav, V., Newman, S., and Sloop, C. D.: Large and
983 seasonally varying biospheric CO₂ fluxes in the Los Angeles megacity revealed by atmospheric radiocarbon, *P. Natl. Acad.*
984 *Sci. Usa.*, 117, 26681-26687, <https://doi.org/10.1073/pnas.2005253117>, 2020.

985 Mitchell, L. E., Lin, J. C., Bowling, D. R., Pataki, D. E., Strong, C., Schauer, A. J., Bares, R., Bush, S. E., Stephens, B. B., and
986 Mendoza, D.: Long-term urban carbon dioxide observations reveal spatial and temporal dynamics related to urban
987 characteristics and growth, *P. Natl. Acad. Sci. Usa.*, 115, 2912-2917, <https://doi.org/10.1073/pnas.1702393115>, 2018.

988 Nalini, K., Lauvaux, T., Abdallah, C., Lian, J., Ciais, P., Utard, H., Laurent, O., and Ramonet, M.: High - resolution Lagrangian
989 inverse modeling of CO₂ emissions over the Paris region during the first 2020 lockdown period, *J. Geophys. Res.-Atmos.*,
990 127, e2021JD036032, <https://doi.org/10.1029/2021JD036032>, 2022.

991 Newman, S., Jeong, S., Fischer, M., Xu, X., Haman, C., Lefer, B., Alvarez, S., Rappenglueck, B., Kort, E., and Andrews, A.:
992 Diurnal tracking of anthropogenic CO₂ emissions in the Los Angeles basin megacity during spring 2010, *Atmos. Chem.*
993 *Phys.*, 13, 4359-4372, <https://doi.org/10.5194/acp-13-4359-2013>, 2013.

994 Pan, C., Zhu, X., Wei, N., Zhu, X., She, Q., Jia, W., Liu, M., and Xiang, W.: Spatial variability of daytime CO₂ concentration
995 with landscape structure across urbanization gradients, Shanghai, China, *Clim. Res.*, 69, 107-116,
996 <https://doi.org/10.3354/cr01394>, 2016.

997 Park, C., Jeong, S., Shin, Y.-s., Cha, Y.-s., and Lee, H.-c.: Reduction in urban atmospheric CO₂ enhancement in Seoul, South
998 Korea, resulting from social distancing policies during the COVID-19 pandemic, *Atmos. Pollut. Res.*, 12, 101176,
999 <https://doi.org/10.1016/j.apr.2021.101176>, 2021.

1000 Pitt, J. R., Lopez-Coto, I., Hajny, K. D., Tomlin, J., Kaeser, R., Jayarathne, T., Stirm, B. H., Floerchinger, C. R., Loughner, C.
1001 P., and Gately, C. K.: New York City greenhouse gas emissions estimated with inverse modeling of aircraft measurements,
1002 *Elem Sci Anth*, 10, 00082, <https://doi.org/10.1525/elementa.2021.00082>, 2022.

1003 Qingdao Municipal Bureau of Statistics: Qingdao Statistical Yearbook 2024, Tech. rep.,
1004 http://qdtj.qingdao.gov.cn/tongjisj/tjsj_tjnj/tjnj_2024/202501/P020250114376271252952.pdf (last access: 1 December
1005 2025), 2024.

1006 Qiu, X. and Fan, S.: Study on the application of auto-meteorological station data in local circulations analysis such as the sea-
1007 land breeze, *Acta Scientiarum Naturalium Universitatis Sunyatseni*, 52(2), 133-136,
1008 <https://doi.org/10.13471/j.cnki.acta.snus.2013.02.025>, 2013.

1009 Reddy, T. R., Mehta, S. K., Ananthavel, A., Ali, S., Annamalai, V., and Rao, D. N.: Seasonal characteristics of sea breeze and
1010 thermal internal boundary layer over Indian east coast region, *Meteorol. Atmos. Phys.*, 133, 217-232,
1011 <https://doi.org/10.1007/s00703-020-00746-1>, 2021.

1012 Sargent, M., Barrera, Y., Nehrkorn, T., Hutyra, L. R., Gately, C. K., Jones, T., McKain, K., Sweeney, C., Hegarty, J., Hardiman,

1013 B., Wang, J. A., and Wofsy, S. C.: Anthropogenic and biogenic CO₂ fluxes in the Boston urban region, *P. Natl. Acad. Sci.*
1014 *Usa.*, 115, 7491-7496, <https://doi.org/10.1073/pnas.1803715115>, 2018.

1015 Schuldt, K. N., Mund, J., Aalto, T., Abshire, J. B., Aikin, K., Allen, G., Andrade, M., Andrews, A., Apadula, F., Arnold, S.,
1016 Baier, B., Bakwin, P., Bartyzel, J., Bentz, G., Bergamaschi, P., Beyersdorf, A., Biermann, T., Biraud, S. C., Blanc, P.-E.,
1017 Boenisch, H., Bowling, D., Brailsford, G., Brand, W. A., Brunner, D., Bui, T. P., Burban, B., Bani, L., Calzolari, F., Chang,
1018 C. S., Chen, H., Chen, G., Chmura, L., Clark, S., Climadat, S., Colomb, A., Commane, R., Condori, L., Conen, F., Conil,
1019 S., Couret, C., Cristofanelli, P., Cuevas, E., Curcoll, R., Daube, B., Davis, K. J., De Mazière, M., De Wekker, S., Dean-Day,
1020 J. M., Della Coletta, J., Delmotte, M., Di Iorio, T., DiGangi, E., DiGangi, J. P., Dickerson, R., Elsasser, M., Emmenegger,
1021 L., Fang, S., Forster, G., France, J., Frumau, A., Fuente-Lastra, M., Galkowski, M., Gatti, L. V., Gehrlein, T., Gerbig, C.,
1022 Gheusi, F., Gloor, E., Goto, D., Griffis, T., Hammer, S., Hanisco, T. F., Hanson, C., Haszpra, L., Hatakka, J., Heimann, M.,
1023 Heliasz, M., Heltai, D., Henne, S., Hensen, A., Hermans, C., Hermansen, O., Hintsa, E., Hoheisel, A., Holst, J., Iraci, L. T.,
1024 Ivakhov, V., Jaffe, D. A., Jordan, A., Joubert, W., Kang, H.-Y., Karion, A., Kawa, S. R., Kazan, V., Keeling, R. F., Keronen,
1025 P., Kim, J., Klausen, J., Kneuer, T., Ko, M.-Y., Kolari, P., Kominkova, K., Kort, E., Kozlova, E., Krummel, P. B., Kubistin,
1026 D., Kulawik, S. S., Kumps, N., Labuschagne, C., Lam, D. H., Lan, X., Langenfelds, R. L., Lanza, A., Laurent, O., Laurila,
1027 T., Lauvaux, T., Lavric, J., Law, B. E., Lee, C.-H., Lee, J., Lehner, I., Lehtinen, K., Leppert, R., Leskinen, A., Leuenberger,
1028 M., Leung, W. H., Levin, I., Levula, J., Lin, J., Lindauer, M., Lindroth, A., Loh, Z. M., Lopez, M., Lunder, C. R., Löfvenius,
1029 M. O., Machida, T., Mammarella, I., Manca, G., Manning, A., Manning, A., Marek, M. V., Marklund, P., Marrero, J. E.,
1030 Martin, M. Y., Martin, D., Martins, G. A., Matsueda, H., McKain, K., Meijer, H., Meinhardt, F., Merchant, L., Metzger, J.-
1031 M., Mihalopoulos, N., Miles, N. L., Miller, C. E., Miller, J. B., Mitchell, L., Monteiro, V., Montzka, S., Moossen, H.,
1032 Moreno, C., Morgan, E., Morgui, J.-A., Morimoto, S., Munger, J. W., Munro, D., Mutuku, M., Myhre, C. L., Mölder, M.,
1033 Müller-Williams, J., Nakaoka, S.-I., Necki, J., Newman, S., Nichol, S., Nisbet, E., Niwa, Y., Njiru, D. M., Noe, S. M., Nojiri,
1034 Y., O'Doherty, S., Obersteiner, F., Paplawsky, B., Parworth, C. L., Peischl, J., Peltola, O., Peters, W., Philippon, C.,
1035 Piacentino, S., Pichon, J. M., Pickers, P., Piper, S., Pitt, J., Plass-Dülmer, C., Platt, S. M., Prinzivalli, S., Ramonet, M.,
1036 Ramos, R., Ren, X., Reyes-Sanchez, E., Richardson, S. J., Rigoulet, L.-J., Riris, H., Rivas, P. P., Rothe, M., Roulet, Y.-A.,
1037 Ryerson, T., Ryoo, J.-M., Sargent, M., Sasakawa, M., Schaefer, H., Scheeren, B., Schmidt, M., Schuck, T., Schumacher, M.,
1038 Seibel, J., Seifert, T., Sha, M. K., Shepson, P., Shin, D., Shook, M., Sloop, C. D., Smale, D., Smith, P. D., Spain, G., St.
1039 Clair, J. M., Steger, D., Steinbacher, M., Stephens, B., Sweeney, C., Sørensen, L. L., Taipale, R., Takatsuji, S., Tans, P.,
1040 Thoning, K., Timas, H., Torn, M., Trisolino, P., Turnbull, J., Vermeulen, A., Viner, B., Vitkova, G., Walker, S., Watson, A.,
1041 Weiss, R., Weyrauch, D., Wofsy, S. C., Worsey, J., Worthy, D., Xueref-Remy, I., Yates, E. L., Young, D., Yver-Kwok, C.,
1042 Zaehle, S., Zahn, A., Zellweger, C., Zimnoch, M., de Souza, R. A., di Sarra, A. G., van Dinter, D., and van den Bulk, P.:
1043 Multi-laboratory compilation of atmospheric carbon dioxide data for the period 1957-2023
1044 (obspack_co2_1_test_GLOBALVIEWplus_v10.1_2024-11-13), NOAA Earth System Research Laboratory, Global
1045 Monitoring Laboratory [dataset], <https://doi.org/10.25925/20241101>, 2024.

1046 Shen, L., Zhao, C., and Yang, X.: Climate - driven characteristics of sea - land breezes over the globe, *Geophys. Res. Lett.*,
1047 48, e2020GL092308, <https://doi.org/10.1029/2020GL092308>, 2021.

1048 Shen, L., Zhao, C., Ma, Z., Li, Z., Li, J., and Wang, K.: Observed decrease of summer sea-land breeze in Shanghai from 1994
1049 to 2014 and its association with urbanization, *Atmos. Res.*, 227, 198-209, <https://doi.org/10.1016/j.atmosres.2019.05.007>,
1050 2019.

1051 Shen, L., Zhao, C., Xu, C., Yan, Y., Chen, A., Yang, Y., Hang, R., Zhu, Y., Zhang, Z., and Song, X.: Effects of sea land breeze
1052 on air - sea turbulent heat fluxes in different seasons using platform observation in East China Sea, *J. Geophys. Res.-Atmos.*,
1053 129, e2023JD040001, <https://doi.org/10.1029/2023JD040001>, 2024.

1054 Shenzhen Municipal Bureau of Statistics: Shenzhen Statistical Yearbook, Tech. rep.,
1055 <https://tjj.sz.gov.cn/attachment/1/1568/1568796/12061198.pdf> (last access: 1 December 2025), 2024.

1056 Shusterman, A. A., Kim, J., Lieschke, K. J., Newman, C., Wooldridge, P. J., and Cohen, R. C.: Observing local CO₂ sources
1057 using low-cost, near-surface urban monitors, *Atmos. Chem. Phys.*, 18, 13773-13785, [https://doi.org/10.5194/acp-18-13773-](https://doi.org/10.5194/acp-18-13773-2018)
1058 [2018](https://doi.org/10.5194/acp-18-13773-2018), 2018.

- 1059 Soininen, J., Kohonen, K.-M., Rantala, P., Kulmala, L., Aaltonen, H., and Järvi, L.: Carbon uptake of an urban green space
1060 inferred from carbonyl sulfide fluxes, *npj Clim Atmos Sci*, 8, <https://doi.org/10.1038/s41612-025-00958-5>, 2025.
- 1061 Stauffer, R. M., Thompson, A. M., Martins, D. K., Clark, R. D., Goldberg, D. L., Loughner, C. P., Delgado, R., Dickerson, R.
1062 R., Stehr, J. W., and Tzortziou, M. A.: Bay breeze influence on surface ozone at Edgewood, MD during July 2011, *J. Atmos.*
1063 *Chem.*, 72, 335-353, <https://doi.org/10.1007/s10874-012-9241-6>, 2015.
- 1064 Sun, L., Tian, W., Zhang, W., Liu, C., and Fang, C.: Characteristics of sea-land breezes and their impact on PM_{2.5} and O₃ in
1065 Shanghai and adjacent areas, *Acta Scientiae Circumstantiae*, 42(9), 339-350, <https://doi.org/10.13671/j.hjkxxb.2022.0111>,
1066 2022.
- 1067 Tianjin Municipal Bureau of Statistics: Tianjin Statistical Yearbook, Tech. rep.,
1068 <https://stats.tj.gov.cn/nianjian/2024nj/zk/indexch.htm> (last access: 1 December 2025), 2024.
- 1069 Turnbull, J. C., Karion, A., Davis, K. J., Lauvaux, T., Miles, N. L., Richardson, S. J., Sweeney, C., McKain, K., Lehman, S. J.,
1070 and Gurney, K. R.: Synthesis of urban CO₂ emission estimates from multiple methods from the Indianapolis Flux Project
1071 (INFLUX), *Environ. Sci. Technol.*, 53, 287-295, <https://doi.org/10.1021/acs.est.8b05552>, 2018.
- 1072 Turnbull, J. C., Sweeney, C., Karion, A., Newberger, T., Lehman, S. J., Tans, P. P., Davis, K. J., Lauvaux, T., Miles, N. L., and
1073 Richardson, S. J.: Toward quantification and source sector identification of fossil fuel CO₂ emissions from an urban area:
1074 Results from the INFLUX experiment, *J. Geophys. Res.-Atmos.*, 120, 292-312, <https://doi.org/10.1002/2014JD022555>,
1075 2015.
- 1076 Turnbull, J. C., Tans, P. P., Lehman, S. J., Baker, D., Conway, T. J., Chung, Y., Gregg, J., Miller, J. B., Southon, J. R., and Zhou,
1077 L. X.: Atmospheric observations of carbon monoxide and fossil fuel CO₂ emissions from East Asia, *J. Geophys. Res.-*
1078 *Atmos.*, 116, <https://doi.org/10.1029/2011JD016691>, 2011.
- 1079 Velasco, E., Roth, M., Tan, S., Quak, M., Nabarro, S., and Norford, L.: The role of vegetation in the CO₂ flux from a tropical
1080 urban neighbourhood, *Atmos. Chem. Phys.*, 13, 10185-10202, <https://doi.org/10.5194/acp-13-10185-2013>, 2013.
- 1081 Verhulst, K. R., Karion, A., Kim, J., Salameh, P. K., Keeling, R. F., Newman, S., Miller, J., Sloop, C., Pongetti, T., and Rao,
1082 P.: Carbon dioxide and methane measurements from the Los Angeles Megacity Carbon Project—Part 1: calibration, urban
1083 enhancements, and uncertainty estimates, *Atmos. Chem. Phys.*, 17, 8313-8341, <https://doi.org/10.5194/acp-17-8313-2017>,
1084 2017.
- 1085 Vimont, I. J., Turnbull, J. C., Petrenko, V. V., Place, P. F., Sweeney, C., Miles, N., Richardson, S., Vaughn, B. H., and White,
1086 J. W.: An improved estimate for the $\delta^{13}\text{C}$ and $\delta^{18}\text{O}$ signatures of carbon monoxide produced from atmospheric oxidation of
1087 volatile organic compounds, *Atmos. Chem. Phys.*, 19, 8547-8562, <https://doi.org/10.5194/acp-19-8547-2019>, 2019.
- 1088 Wang, B., Geddes, J. A., Adams, T. J., Lind, E. S., McDonald, B. C., He, J., Harkins, C., Li, D., and Pfister, G. G.: Implications
1089 of sea breezes on air quality monitoring in a coastal urban environment: Evidence from high resolution modeling of NO₂
1090 and O₃, *J. Geophys. Res.-Atmos.*, 128, e2022JD037860, <https://doi.org/10.1029/2022JD037860>, 2023.
- 1091 Wang, P., Zhou, W., Niu, Z., Xiong, X., Wu, S., Cheng, P., Hou, Y., Lu, X., and Du, H.: Spatio-temporal variability of
1092 atmospheric CO₂ and its main causes: A case study in Xi'an city, China, *Atmos. Res.*, 249, 105346,
1093 <https://doi.org/10.1016/j.atmosres.2020.105346>, 2021.
- 1094 Wang, P., Zhou, W., Xiong, X., Wu, S., Niu, Z., Yu, Y., Liu, J., Feng, T., Cheng, P., and Du, H.: Source attribution of atmospheric
1095 CO₂ using ¹⁴C and ¹³C as tracers in two Chinese megacities during winter, *J. Geophys. Res.-Atmos.*, 127, e2022JD036504,
1096 <https://doi.org/10.1029/2022JD036504>, 2022.
- 1097 Wang, Y., Munger, J., Xu, S., McElroy, M. B., Hao, J., Nielsen, C., and Ma, H.: CO₂ and its correlation with CO at a rural site
1098 near Beijing: implications for combustion efficiency in China, *Atmos. Chem. Phys.*, 10, 8881-8897,
1099 <https://doi.org/10.5194/acp-10-8881-2010>, 2010.
- 1100 Wei, D., Reinmann, A., Schiferl, L. D., and Commane, R.: High resolution modeling of vegetation reveals large summertime
1101 biogenic CO₂ fluxes in New York City, *Environ. Res. Lett.*, 17, 124031, <https://doi.org/10.1088/1748-9326/aca68f>, 2022.
- 1102 WMO: WMO Greenhouse Gas Bulletin No. 20 – The State of Greenhouse Gases in the Atmosphere Based on Global
1103 Observations through 2023, Tech. rep., <https://library.wmo.int/idurl/4/69057> (last access: 18 June 2025), 2024.
- 1104 WMO: GAW Report No. 314 – Integrated Global Greenhouse Gas Information System: Urban Emission Observation and

1105 Monitoring Good Research Practice Guidelines, Tech. rep., <https://library.wmo.int/idurl/4/69623> (last access: 1 December
1106 2025), 2025.

1107 Wu, D., Lin, J. C., Duarte, H. F., Yadav, V., Parazoo, N. C., Oda, T., and Kort, E. A.: A model for urban biogenic CO₂ fluxes:
1108 Solar-Induced Fluorescence for Modeling Urban biogenic Fluxes (SMUrF v1), *Geosci. Model Dev.*, 14, 3633-3661,
1109 <https://doi.org/10.5194/gmd-14-3633-2021>, 2021.

1110 Wu, D., Liu, J., Wennberg, P. O., Palmer, P. I., Nelson, R. R., Kiel, M., and Eldering, A.: Towards sector-based attribution
1111 using intra-city variations in satellite-based emission ratios between CO₂ and CO, *Atmos. Chem. Phys.*, 22, 14547-14570,
1112 <https://doi.org/10.5194/acp-22-14547-2022>, 2022a.

1113 Wu, K., Davis, K. J., Miles, N. L., Richardson, S. J., Lauvaux, T., Sarmiento, D. P., Balashov, N. V., Keller, K., Turnbull, J.,
1114 and Gurney, K. R.: Source decomposition of eddy-covariance CO₂ flux measurements for evaluating a high-resolution
1115 urban CO₂ emissions inventory, *Environ. Res. Lett.*, 17, 074035, <https://doi.org/10.1088/1748-9326/ac7c29>, 2022b.

1116 Wu, M., Wu, D., Fan, Q., Wang, B. M., Li, H. W., and Fan, S. J.: Observational studies of the meteorological characteristics
1117 associated with poor air quality over the Pearl River Delta in China, *Atmos. Chem. Phys.*, 13, 10755-10766,
1118 <https://doi.org/10.5194/acp-13-10755-2013>, 2013.

1119 Xiao, Y., Yang, J., Cui, L., Deng, J., Fu, P., and Zhu, J.: Weakened Sea - Land Breeze in a Coastal Megacity Driven by
1120 Urbanization and Ocean Warming, *Earth's Future*, 11, e2022EF003341, <https://doi.org/10.1029/2022EF003341>, 2023.

1121 Xu, R., Tong, D., Xiao, Q., Qin, X., Chen, C., Yan, L., Cheng, J., Cui, C., Hu, H., and Liu, W.: MEIC-global-CO₂: A new
1122 global CO₂ emission inventory with highly-resolved source category and sub-country information, *Sci. China Earth Sci*, 67,
1123 450-465, <https://doi.org/10.1007/s11430-023-1230-3>, 2024.

1124 Xueref-Remy, I., Dieudonné, E., Vuillemin, C., Lopez, M., Lac, C., Schmidt, M., Delmotte, M., Chevallier, F., Ravetta, F.,
1125 Perrussel, O., Ciais, P., Bréon, F.-M., Broquet, G., Ramonet, M., Spain, T. G., and Ampe, C.: Diurnal, synoptic and seasonal
1126 variability of atmospheric CO₂ in the Paris megacity area, *Atmos. Chem. Phys.*, 18, 3335-3362, <https://doi.org/10.5194/acp-18-3335-2018>, 2018.

1128 Yadav, V., Ghosh, S., Mueller, K., Karion, A., Roest, G., Gourdji, S. M., Lopez - Coto, I., Gurney, K. R., Parazoo, N., and
1129 Verhulst, K. R.: The impact of COVID - 19 on CO₂ emissions in the Los Angeles and Washington DC/Baltimore
1130 metropolitan areas, *Geophys. Res. Lett.*, 48, e2021GL092744, <https://doi.org/10.1029/2021GL092744>, 2021.

1131 Yang, H., Wu, K., Shen, H., Janssens-Maenhout, G., Crippa, M., Guizzardi, D., and Zhou, M.: A comparative analysis of
1132 China's anthropogenic CO₂ emissions (2000–2023): insights from six bottom-up inventories and uncertainty assessment,
1133 *Atmos. Chem. Phys.*, 25, 18111-18127, <https://doi.org/10.5194/acp-25-18111-2025>, 2025.

1134 Yang, J. and Huang, X.: The 30 m annual land cover datasets and its dynamics in China from 1985 to 2024, *Earth System
1135 Science Data [dataset]*, <https://doi.org/10.5281/zenodo.15853565>, 2025.

1136 Yang, T., Li, H. Y., Cao, J., Lu, Q. Q., Wang, Z. F., He, L. T., Sun, H. H., and Han, K.: Investigating the climatology of North
1137 China's urban inland lake based on six years of observations, *Sci. Total Environ.*, 826,
1138 <https://doi.org/10.1016/j.scitotenv.2022.154120>, 2022.

1139 Yang, Y., Zhou, M., Wang, T., Yao, B., Han, P., Ji, D., Zhou, W., Sun, Y., Wang, G., and Wang, P.: Spatial and temporal
1140 variations of CO₂ mole fractions observed at Beijing, Xianghe, and Xinglong in North China, *Atmos. Chem. Phys.*, 21,
1141 11741-11757, <https://doi.org/10.5194/acp-21-11741-2021>, 2021.

1142 Ye, X., Lauvaux, T., Kort, E. A., Oda, T., Feng, S., Lin, J. C., Yang, E. G., and Wu, D.: Constraining fossil fuel CO₂ emissions
1143 from urban area using OCO - 2 observations of total column CO₂, *J. Geophys. Res.-Atmos.*, 125, e2019JD030528,
1144 <https://doi.org/10.1029/2019JD030528>, 2020.

1145 You, C. and Chi-Hung Fung, J.: Characteristics of the Sea-Breeze Circulation in the Pearl River Delta Region and Its
1146 Dynamical Diagnosis, *J. Appl. Meteorol. Clim.*, 58, 741-755, <https://doi.org/10.1175/jamc-d-18-0153.1>, 2019.

1147 Young, H. A., Turnbull, J. C., Keller, E. D., Domingues, L. G., Parry-Thompson, J., Hilton, T. W., Brailsford, G. W., Gray, S.,
1148 Moss, R. C., and Mikaloff-Fletcher, S.: Urban flask measurements of CO₂ff and CO to identify emission sources at different
1149 site types in Auckland, New Zealand, *Philosophical Transactions of the Royal Society A*, 381, 20220204,
1150 <https://doi.org/10.1098/rsta.2022.0204>, 2023.

1151 Zhang, L., Lin, J., Shao, Y., Huang, S., Fan, S., and Wei, W.: Understanding the impact of sea and land breezes on ozone
1152 pollution in the Pearl River Delta, *Acta Scientiae Circumstantiae*, 44(1), 74-85, <https://doi.org/10.13671/j.hjkxxb.2023.0285>,
1153 2024.

1154 Zhao, D., Xin, J., Wang, W., Jia, D., Wang, Z., Xiao, H., Liu, C., Zhou, J., Tong, L., and Ma, Y.: Effects of the sea-land breeze
1155 on coastal ozone pollution in the Yangtze River Delta, China, *Sci. Total Environ.*, 807, 150306,
1156 <https://doi.org/10.1016/j.scitotenv.2021.150306>, 2022.

1157 Zheng, B., Tong, D., Li, M., Liu, F., Hong, C., Geng, G., Li, H., Li, X., Peng, L., Qi, J., Yan, L., Zhang, Y., Zhao, H., Zheng,
1158 Y., He, K., and Zhang, Q.: Trends in China's anthropogenic emissions since 2010 as the consequence of clean air actions,
1159 *Atmos. Chem. Phys.*, 18, 14095-14111, <https://doi.org/10.5194/acp-18-14095-2018>, 2018.

1160 Zheng, Y., Jiang, F., Feng, S., Shen, Y., Liu, H., Guo, H., Lyu, X., Jia, M., and Lou, C.: Large-scale land-sea interactions extend
1161 ozone pollution duration in coastal cities along northern China, *Env. Sci. Ecotechnol.*, 18, 100322,
1162 <https://doi.org/10.1016/j.ese.2023.100322>, 2024.

1163